Journal of Vibration Engineering & Technologies (2024) 12:5811–5833
https://doi.org/10.1007/s42417-023-01220-z

ORIGINAL PAPER

Nonlinear Dynamic Analysis of Herringbone Gears Transmission

Shuai Mo[1,2,3,4] · **Yanjun Zeng**[1,2] · **Zhen Wang**[1,2] · **Wei Zhang**[1]

Received: 26 September 2023 / Revised: 7 November 2023 / Accepted: 12 November 2023 / Published online: 12 December 2023

Abstract

Purpose The herringbone gears can eliminate the additional axial load during the meshing process of helical gears, and make the meshing more stable. Therefore, it is widely used in gear transmission systems. Analyzing the nonlinear characteristics of the gear system will be beneficial to the design work.

Methods The nonlinear dynamic model of the herringbone gears transmission system is established, the fourth-order Runge–Kutta integral method is used to solve the differential equations of system dynamics under different external load excitation frequencies, and using the multi-scale method, the system's primary resonance response and the stability conditions of the main resonance have been analyzed. The main resonance characteristics are analyzed by numerical method.

Results When the external excitation frequency and torque are gradually increased, and the meshing stiffness and damping are gradually reduced, the motion state of the system gradually changes from stable single-cycle motion state to chaotic state. Gradually increasing the meshing damping and meshing stiffness, the unstable branch of the amplitude–frequency characteristic curve gradually shrinks and eventually disappears.

Conclusions The system exhibits nonlinear motion characteristics under external excitation. To control the main common amplitude value and ensure the stability of the system, the system parameters, such as meshing damping and external load amplitude, should be reasonably selected.

Keywords Nonlinear dynamics · Time-varying mesh stiffness · Bifurcation and chaos · Multi-scale · Primary resonance

Introduction

The herringbone gear is composed of a pair of symmetrical helical gears and an intermediate shaft segment. It can eliminate the additional axial load during the meshing process of helical gears, increase the contact ratio, and make the meshing more stable. Therefore, it is widely used in gear transmission systems. The nonlinear characteristics of the gear system are analyzed, the influence of various factors on nonlinear behavior is explored, and the stable operation interval is found, this will be beneficial to the design work.

Research of the system's nonlinear characters has been conducted deeply by Substantial scholars. They [1–11] established and solved the nonlinear dynamic model of the system considering the influence of time-varying meshing stiffness, pitch deviation, backlash, and tooth center deviation. The double planetary gear sets (DPGSs) have excellent performance and is widely used in the transmission system. In previous studies, the time-varying gear excitation is often ignored, which makes the vibration characteristic analysis results inaccurate. Liu [12, 13] establishes the

Shuai Mo and Yanjun Zeng contributed equally to this work, they are co-first authors of the article.

✉ Shuai Mo
moshuai2010@163.com

✉ Wei Zhang
sandyzhang9@163.com

[1] State Key Laboratory of Featured Metal Materials and Life-Cycle Safety for Composite Structures, Guangxi University, Nanning 530004, China

[2] School of Mechanical Engineering, Guangxi University, Nanning 530004, China

[3] State Key Lab of Digital Manufacturing Equipment and Technology, Huazhong University of Science and Technology, Wuhan 430074, China

[4] National Key Laboratory of Science and Technology On Helicopter Transmission, Nanjing 210016, China

dynamic model of the flexible shaft gear transmission system (FGDS) and the dynamic model of the double planetary gear set (DPGS). The theoretical analysis and experimental verification are combined to study the nonlinear dynamic characteristics of the time-varying excitation force of the system through the acceleration map, spectrum map and other images. Xu [14] takes the tooth surface friction into account, to study the system dynamic response, propose a dynamic model of new HPGS coupling. Mo [15–19] established a face gear model, in which the axis of the gear is not perpendicular to each other, and studied its nonlinear dynamic response by cell mapping method. Wang [20, 21] established the improved GTF aero-engine gear–rotor coupling transmission system nonlinear dynamic model considering multiple nonlinear parameters and studied the influence of bifurcation parameters, such as damping ratio and comprehensive meshing error on the dynamic response of the system. Tian [22] considered the time-varying contact stiffness, clearance of bearing and backlash, establish the motion model of coupling. The complex nonlinear behaviors of the system were revealed by the bifurcation diagram, time domain diagram, Poincare section diagram and phase plane diagram.

The multi-scale method includes analysis methods, such as primary resonance analysis, super-harmonic analysis, and sub-harmonic analysis. It usually decomposes the differential equation solution into multiple time-scale functions, which can effectively improve the calculation accuracy and has broad applications in various research fields. Wang et al. [23] derived the displacement and voltage frequency response functions of the monostable energy harvester based on the harmonic balance expansion method and the multi-scale method, respectively. Jian [24] established an active control system model with time delay feedback, analyzed the stability of the system by an effective method. Huang [25] and other scholars established the dynamic model of a high-speed train gear transmission system under stick–slip oscillation, listed the super-harmonic resonance frequency response equation of the system by multi-scale method, and analyzed the stability of the system by perturbation theory. Many scholars [26–32] consider plurality system nonlinear factors that exist in engineering practice and introduce them, then system nonlinear dynamic model can be established, and carried out a multi-scale analysis of the main resonance characteristics of the system to determine the stable operation region of the system.

The nonlinear vibration and primary resonance response of herringbone gear transmission systems considering time-varying meshing stiffness, clearance of tooth side, error of transmission, clearance of bearing, and other factors is what this paper mainly focuses on. The main content of the article can be divided into the following parts: in the first part, to analyze the nonlinear meshing force on the gear, the error of meshing and the backlash are selected to introduce in the actual existence of many nonlinear factors. In the actual production, bearing will have clearance, which should be introduced to establish the nonlinear vibration dynamic model of bearing and calculate the force in the bearing. The system components dynamic analysis is carried out, and the calculation method and numerical images at different times of the system time-varying stiffness of gears meshing is given. Second, the second part establishes the system dynamics model, lists the vibration differential equations, and performs dimensionless processing. Subsequently, the third part solves an example and studies the influence of excitation frequency on the nonlinear behavior of the system through a time domain diagram, frequency domain diagram, phase diagram, Poincare section, and bifurcation diagram. In the fourth part, using the multi-scale method, one of the characteristics of the herringbone gear transmission system-stability conditions has been derived. Using the numerical method, how will the changing of meshing damping and load excitation influence the amplitude–frequency characteristics of the system have been simulated, this is beneficial to establish the stable operation interval of the system. Finally, the conclusion is drawn in the fifth part. The workflow of the research is shown in Fig. 1.

Dynamics Analysis of System Components

Meshing Line Displacement and Meshing Force

Taking the right helical gear pair as an example, the meshing line displacement is calculated by the following equation:

$$x_{n1} = (x_1 - x_2)\sin\alpha_n + (y_1 - y_2)\cos\alpha_n\cos\beta + (z_1 - z_2)\cos\alpha_n\sin\beta + (R_{b1}\theta_1 - R_{b2}\theta_2)\cos\alpha_n\cos\beta - e(t). \tag{1}$$

In the formula, x_1, y_1, z_1, θ_1 is The vibration displacement and torsional displacement of the right active helical gear; x_2, y_2, z_2, θ_2 is The vibration displacement and torsional displacement of the right driven helical gear in each direction; α_n, β are the normal pressure angle and spiral angle, respectively. $e(t)$ is the static transfer error, calculated by the following equation:

$$e(t) = e\sin\omega_m t. \tag{2}$$

In the formula, e is the mean value of static transmission error, and ω_m is the meshing frequency of the helical gear pair, which is equal to the product of helical gear rotation frequency and tooth number.

Express the backlash nonlinear function in the following equation:

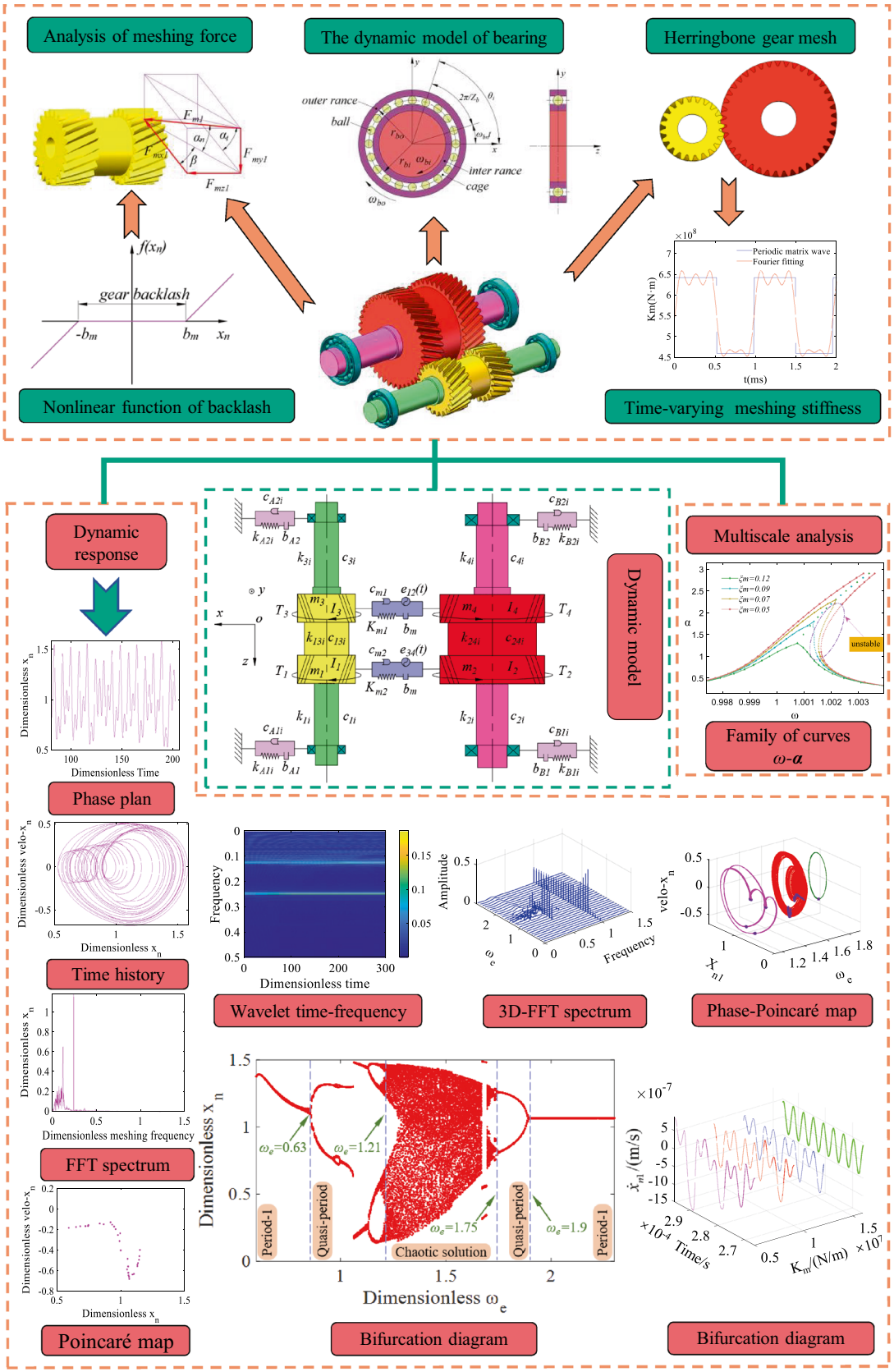

Fig. 1 Structure flow chart of nonlinear dynamic analysis

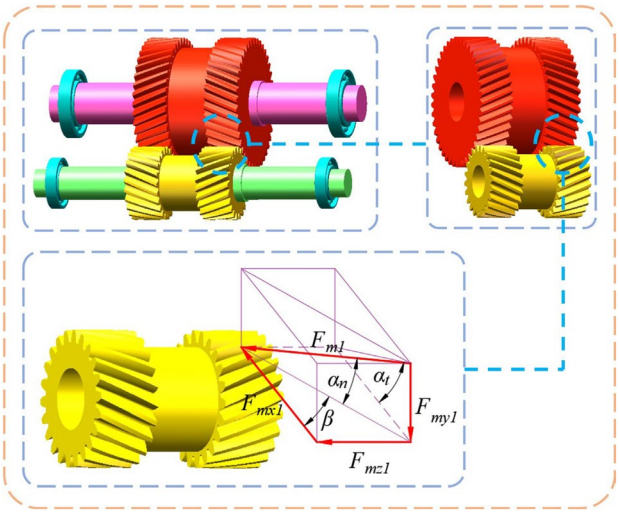

Fig. 2 Meshing force of herringbone gear

$$f(x_{n1}) = \begin{cases} x_{n1} - b_m, & x_{n1} > b_m \\ 0, & |x_{n1}| < b_m \\ x_{n1} + b_m, & x_{n1} < -b_m \end{cases}. \tag{3}$$

In the formula, b_m is half of the tooth side clearance value.

The calculation formula of meshing force is shown in the following formula:

$$F_{m1} = K_m(t) f(x_{n1}) + C_m \dot{x}_{n1}. \tag{4}$$

In the formula, $K_m(t)$ is the time-varying meshing stiffness of the helical gear pair, and C_m is the meshing damping. The force of the gear meshing process is shown in Fig. 2.

According to the above relationship, the calculation formula of meshing force is obtained, as shown in the following formula:

$$\begin{cases} F_{mx1} = F_{m1} \sin \alpha_n \\ F_{my1} = F_{m1} \cos \alpha_n \cos \beta \\ F_{mz1} = F_{m1} \cos \alpha_n \sin \beta \end{cases}. \tag{5}$$

The calculation method of the meshing force of the left helical gear pair is the same.

Time-Varying Meshing Stiffness and Damping

Approximating the meshing stiffness of the gear pair as a rectangular wave. The calculation method is as follows:

According to ISO6336-2006, the calculation formula of single tooth meshing stiffness is:

$$C' = c_{\text{th}}' C_M C_R C_B B \cos \beta \tag{6}$$

In the formula, β is the helix angle, B is the tooth width, c_{th}' can be calculated by the following formula:

$$\begin{cases} c'_{th} = \dfrac{1}{q'} \\ q' = C_1 + \dfrac{C_2}{z_{n1}} + \dfrac{C_3}{z_{n2}} + C_4 x_1^* + \dfrac{C_5 x_1}{z_{n1}} + C_6 x_2^* + \dfrac{C_7 x_2}{z_{n2}} \end{cases}. \tag{7}$$

In Eq. (2), the values of each coefficient are shown in Table 1. Because the helical gear has no displacement, so $x_1 = x_2 = 0$.

C_M is an experimental correction coefficient to measure the difference between the measured value and the theory, usually 0.8. C_R reflects the flexibility of the rim and web, generally 1.0. C_B is the basic rack correction coefficient, $C_{\gamma\alpha}$ is double tooth meshing stiffness, and ε_α is gear contact ratio, the calculation method are shown in the following equation:

$$\begin{cases} C_B = [1 + 0.5(1.25 - h_{fp}/m_n)][1 - 0.02(20° - \alpha_n)] \\ C_{\gamma\alpha} = C'(0.75\varepsilon_\alpha + 0.25) \\ \varepsilon_\alpha = [z_{n1}(\tan \alpha_{a1} - \tan \alpha_n) + z_{n2}(\tan \alpha_{a2} - \tan \alpha_n)]/2\pi \end{cases}. \tag{8}$$

In the formula, h_{fp} is tooth dedendum, m_n is normal-mode propagation module, and α_n is normal pressure angle. α_{a1}, α_{a2} is the Tooth tip circular pressure angle.

The calculation formula of $K_{mi}(t)$ $(i = 1, 2)$ is

$$K_{mi}(t) = \begin{cases} C_{\gamma\alpha} & 0 \le t \le (\varepsilon_\alpha - 1)T \\ C' & (\varepsilon_\alpha - 1)T \le t \le T \end{cases}. \tag{9}$$

In the formula, T is the meshing stiffness variation period. To make the curve of meshing stiffness who has time-varying characteristic more accurate, expand the wave by the Fourier series. Δk_{sn} is the stiffness variation, ω_l is the meshing frequency, a_{sn}^l and b_{sn}^l are the Fourier coefficient, γ_{sn} is the Axis intersection angle, ε_α is the Coincidence degree, Fourier series Order is represented by l, and The 5th order

Table 1 Coefficients of polynomials

C_1	C_2	C_3	C_4	C_5	C_6	C_7
0.04723	0.15551	0.25791	− 0.00635	− 0.11654	− 0.00193	− 0.24188

accuracy is enough. The stiffness calculation method is shown in Formulas (10) and (11):

$$\begin{cases} K_{mi}(t) = k + \Delta k_{sn}(t) \\ k = C_{\gamma\alpha}(\varepsilon_\alpha - 1) + C'(2 - \varepsilon_\alpha) \\ \Delta k_{sn}(t) = \sum_{l=1}^{\infty} (a_{sn}^l \cos l\omega_l t + b_{sn}^l \sin l\omega_l t) \end{cases} \tag{10}$$

$$\begin{cases} b_{sn}^l = k^*\{2\sin\pi l(2\gamma_{sn} + \varepsilon_\alpha - 1)\sin\pi l(\varepsilon_\alpha - 1) + (1 - \varepsilon_\alpha)[\cos 2\pi l(2 - \gamma_{sn} - \varepsilon_\alpha) - 1]\} \\ a_{sn}^l = k^*[2\cos\pi l(2\gamma_{sn} + \varepsilon_\alpha - 1)\sin\pi l(\varepsilon_\alpha - 1) + (1 - \varepsilon_\alpha)[\sin 2\pi l(2 - \gamma_{sn} - \varepsilon_\alpha)] \\ k^* = \dfrac{c_{\gamma\alpha} - c'}{1.6l\pi}. \end{cases} \tag{11}$$

The time-varying meshing stiffness curves of meshing line 1 and meshing line 2 are shown in Fig. 3.

The meshing damping c_m is calculated as follows:

$$c_m = 2\xi\sqrt{\frac{K_m R_p^2 R_g^2 J_P J_g}{R^2 J_p + R_g^2 J_g}}. \tag{12}$$

In the formula, ξ is the damping coefficient, usually 0.03–0.17, J_p and J_g are the rotational inertia of the driving gear and the driven gear, respectively, and R_p and R_g are the radius of the dividing circle of the driving gear and the driven gear, respectively.

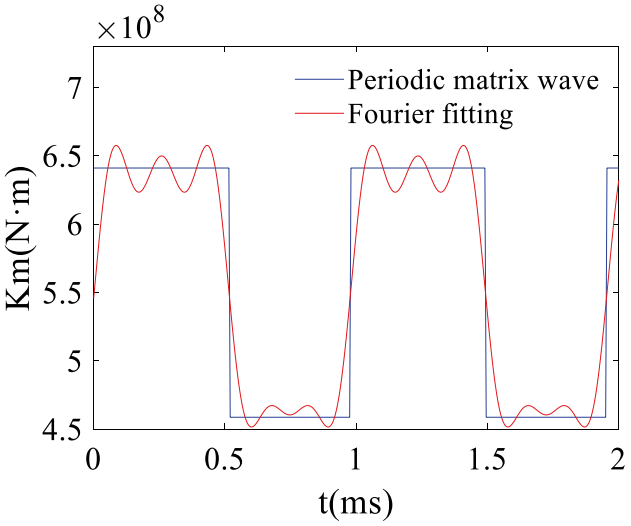

Fig. 3 Time-varying meshing stiffness of each meshing line

Bearing Force Calculation

In the process of establishing the herringbone gears system, the bearings being used are deep groove ball bearings. The structure and coordinate system establishment method are shown in Fig. 4.

What the rotating shaft connects to is the inner ring of the bearing, and the bearing seat is what the outer ring is fixed to. The bearing coordinate system has its own origin, the center of curvature of the inner ring is where it is located. The rotating shaft has its own axis, which is coincides with Z axis.

In the raceway, the rolling elements is assumed that being arranged equidistantly and do not have relative sliding. There

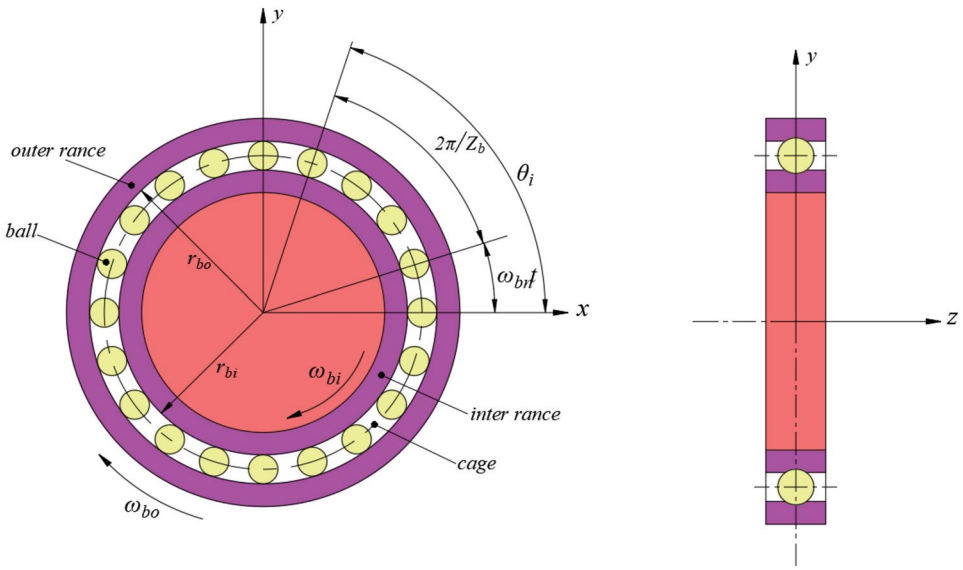

Fig. 4 Bearing model of the herringbone gears system

are contact points between rolling element and rings, whose linear velocity can be calculated by the following formula:

$$\begin{cases} v_{bi} = \omega_{bi} \cdot r_{bi} \\ v_{bo} = \omega_{bo} \cdot r_{bo} \end{cases}. \tag{13}$$

In the formula, ω_{bi} and ω_{bo} are the angular velocities of the inner and outer rings, and r_{bi} and r_{bo} are the radii of the inner and outer rings of the bearing, respectively. What the bearing seats connect to is the outer rings, so $\omega_{bo}=0$, that is, $v_{bo}=0$.

The revolution angular velocity of the rolling element around the axis of the rotating shaft is calculated by the following formula:

$$\omega_{bn} = \frac{v_{bi} + v_{bo}}{r_{bi} + r_{bo}} = \frac{\omega_{bi} \cdot r_{bi}}{r_{bi} + r_{bo}}. \tag{14}$$

The position angle of the rolling element changes with time, and its calculation method is given by the following equation:

$$\theta_i(t) = \frac{2\pi(i-1)}{Z_b} + \omega_{bn} t \quad (i = 1, 2, \ldots Z_b). \tag{15}$$

In the formula, Z_b is the number of rolling elements in the bearing.

The deformation of the bearing rolling element is shown in Fig. 5. When not deformed, O_{bo}, O_{bi} represent outer and inner raceway curvature center of the bearing, respectively, r_{bo} and r_{bi} represent the radius of curvature,

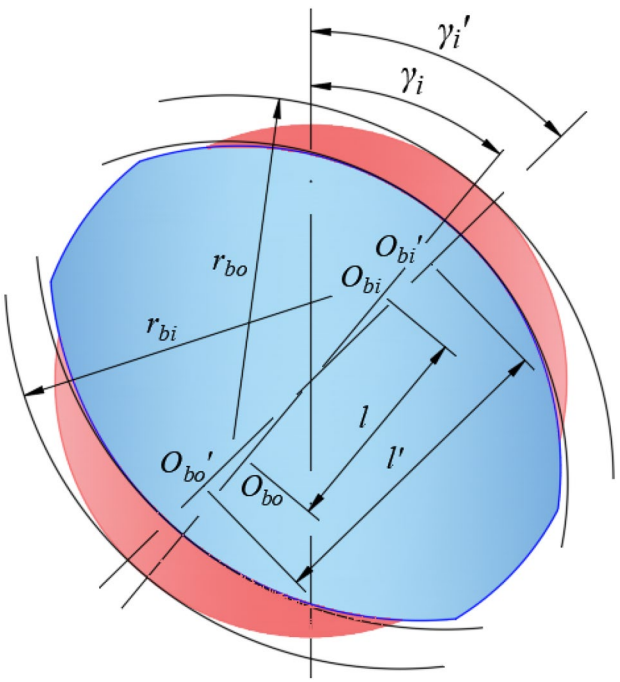

Fig. 5 Rolling deformation diagram

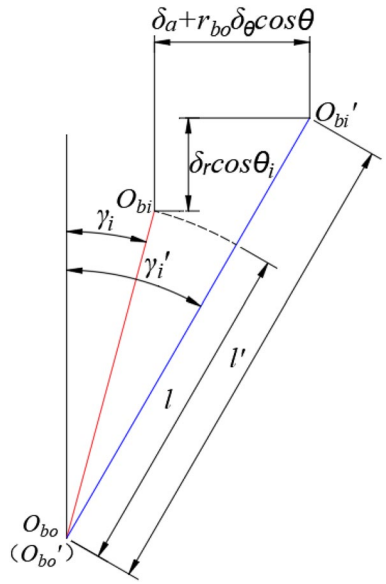

Fig. 6 Geometric relationship diagram

respectively. γ_i represents the contact angle between the rolling element and the outer raceway and the inner raceway when the rolling element is not deformed, and γ_i' represents the contact angle between the deformed rolling element and the outer raceway and the inner raceway. As shown in Fig. 6, because the seat of bearing is connected with the outer ring, it is considered that the center of curvature does not change after the outer ring is stressed. that is, O_{bo} and O_{bo}' are in the same position, and inner ring also changes its curvature center from O_{bi} to O_{bi}'.

Along the coordinate axis, there are displacement of the bearing, which is the factor that should be considered to calculated center distance of the curvature center of both rings after deformation, after deforming, there will be deformation angle in the rolling element, it can be calculated by the following formula:

$$\begin{cases} l' = \sqrt{(l\sin\gamma_i + z + r_{bo}\delta_\theta \cos\theta_i)^2 + \left(y\sin\theta_i + l\cos\gamma_i + x\cos\theta_i\right)^2} \\ \tan\gamma_i' = \dfrac{l\sin\gamma_i + z + r_{bo}\delta_\theta\cos\theta_i}{y\sin\theta_i + l\cos\gamma_i + x\cos\theta} \end{cases}. \tag{16}$$

In the formula, x, y, and z is the vibration displacement of the bearing along the corresponding direction of the coordinate axis.

Taking c as the radial clearance of the bearing, the deformation of the rolling element is calculated by the following formula:

$$\delta = l' - l - c. \tag{17}$$

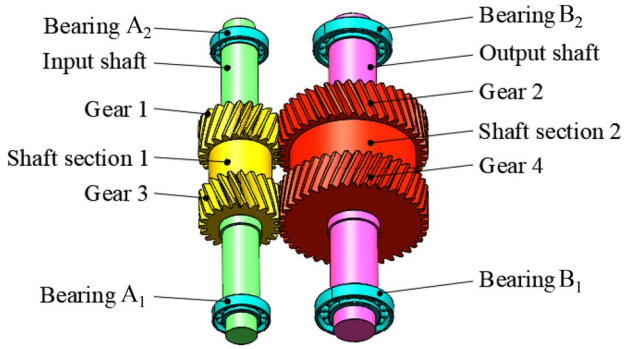

Fig. 7 Three-dimensional model of herringbone gears

Table 2 Basic parameters of the whole system

Serial number	Parameters	Values
1	Eccentric error amplitude (m)	1×10^{-6}
2	Gear backlash (m)	1×10^{-6}
3	Bearing clearance (m)	3×10^{-5}

When the rolling element deformation $\delta>0$, the bearing force will exist, so the Heaviside function is introduced, as shown in Eq. (19):

$$H(\delta)=\begin{cases}1, & \delta>0\\ 0, & \delta<0\end{cases}. \tag{18}$$

The force calculation method of a single rolling element is shown in formula (20), where F_{ab} is the axial force of the rolling element, F_{rb} is the radial force of the rolling element, and K_b is the contact stiffness between the rolling element and the raceway, the calculation method is as follows:

$$\begin{cases}K_b=3.217\times10^5(\delta^*)^{-3/2}\delta_c^{1/2}\left(\sum\rho\right)^{-1/2}\\ \delta^*=\dfrac{2\Gamma(e)}{\pi}\left(\dfrac{\pi(1-e^2)}{2\prod(e)}\right)^{1/3}\end{cases}. \tag{19}$$

In the formula, δ_c is the juxtaposition metamorphosis, $\sum\rho$ is the auxiliary function of raceway contact point. When the bearing is a ball bearing, take $n=2/3$, when the bearing is a roller bearing, take $n=9/10$:

$$\begin{cases}F_{ab}=K_b\delta^n\sin\gamma_i'\cdot H(\delta)\\ F_{rb}=K_b\delta^n\cos\gamma_i'\cdot H(\delta)\end{cases}. \tag{20}$$

The force of a single bearing is expressed as

$$F_{bx}=\sum_{i=1}^{Z_b}F_{rb}\cos\theta_i,\ F_{by}=\sum_{i=1}^{Z_b}F_{rb}\sin\theta_i,\ F_{bz}=\sum_{i=1}^{Z_b}F_{ab}. \tag{21}$$

Table 3 Basic parameters of herringbone gears

	Gear 1	Gear 2	Gear 3	Gear 4
Number of teeth	22	41	22	41
Quality (kg)	5.35	14.87	5.35	14.87
Modulus (mm)	5	5	5	5
Pressure angle (°)	20	20	20	20
Helix angle (°)	22	22	22	22
Tooth width (mm)	60	60	60	60

Table 4 Basic parameters of bearings

	Outer diameter (mm)	Inner diameter (mm)	Width (mm)	Number of rollers
Bearing A_1 & A_3	45	85	19	16
Bearing B_1 & B_2	55	95	21	16

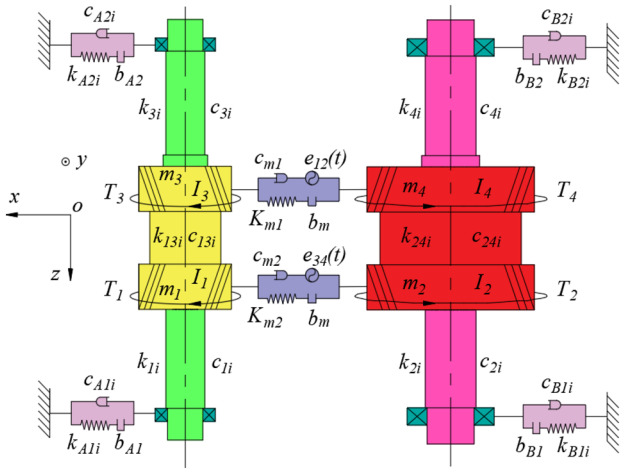

Fig. 8 Vibration model of herringbone gear transmission system

Dynamic Model of Herringbone Gear

Herringbone gears system is composed of an input shaft, an output shaft, four bearings of input and output shaft, respectively, and a pair of herringbone gears. Its three-dimensional model is shown in Fig. 7.

To study the nonlinear behavior of herringbone gears system under certain conditions, the initial parameters of the system are defined, as shown in Table 2, 3, and 4.

The multi-degree-of-freedom coupling vibration model of the single-stage herringbone gear transmission system shown in Fig. 8 is constructed. The herringbone gears are regarded as combinations of four helical gears and two intermediate shaft segments. Herringbone gears system vibration

model takes backlash, the error of transmission, nonlinear vibration of bearing, input torque fluctuation, time-varying stiffness of meshing gears into account while being established. In the diagram, m_1, m_3, I_1, I_3 is the active helical gear mass and moment of inertia on the right and left sides, respectively, and m_2, m_4, I_2, I_4 are the driven helical gear mass and moment of inertia on the right and left sides, respectively. m_{A1} and m_{A2} are the bearing mass on the right and left sides of the input shaft, respectively, and m_{B1} and m_{B2} are the bearing mass on the right and left sides of the output shaft, respectively. k_{A1i}, k_{A2i}, k_{B1i}, k_{B2i}, c_{A1i}, c_{A2i}, c_{B1i}, c_{B2i} $(i=x, y)$ are the stiffness and damping of each bearing inner ring. k_{1i}, k_{2i}, k_{3i}, k_{4i}, c_{1i}, c_{2i}, c_{3i}, c_{4i} $(i=x, y, z, \theta)$ are the stiffness and damping of gear and bearing connecting shaft. k_{13i}, k_{24i}, c_{13i}, c_{24i} $(i=x, y, z, \theta)$ are the stiffness and damping of the intermediate shaft.

The gears are regarded as mass points, their mass is concentrated at the centric. The bearing and the rotating shaft are rigidly connected, so the bearing and the rotating shaft on the same side are regarded as the mass concentrated at the centric. The force on the bearing raceway and the gear meshing force can be decomposed in x, y and z directions. The system considers 24 degrees of freedom:

$$\{x_1, y_1, z_1, \theta_1, x_2, y_2, z_2, \theta_2, x_3, y_3, z_3, \theta_3, x_4, y_4, z_4, \theta_4, x_{A1}, y_{A1}, x_{A2}, y_{A2}, x_{B1}, y_{B1}, x_{B2}, y_{B2}\}.$$

Among them, x_i, y_i, z_i, θ_i $(i=1, 2, 3, 4)$ are the vibration and torsional displacement of each helical gear, x_{vj}, y_{vj} $(v=A, B; j=1, 2)$ are the radial and tangential displacements of each bearing.

The system vibration differential equation is as follows:

$$\begin{cases} m_1\ddot{x}_1 + c_{x1}(\dot{x}_1 - \dot{x}_{A1}) + c_{x13}(\dot{x}_1 - \dot{x}_3) + k_{x1}(x_1 - x_{A1}) + k_{x13}(x_1 - x_{A1}) \\ = -F_{mx1} \\ m_1\ddot{y}_1 + c_{y1}(\dot{y}_1 - \dot{y}_{A1}) + c_{y13}(\dot{y}_1 - \dot{y}_3) + k_{y1}(y_1 - x_{A1}) + k_{y13}(y_1 - y_{A1}) \\ = -F_{my1} - m_{A1}g + F_1 \\ m_1\ddot{z}_1 + c_{z1}(\dot{z}_1 - \dot{z}_{A1}) + c_{z13}(\dot{z}_1 - \dot{z}_3) + k_{z1}(z_1 - z_{A1}) + k_{z13}(z_1 - z_{A1}) = F_{mz1} \\ I_1\ddot{\theta}_1 + c_{t13}(\dot{\theta}_1 - \dot{\theta}_3) + c_{t1}\dot{\theta}_1 + k_{t13}(\theta_1 - \theta_3) + k_{t1}\theta_1 = T_1 \\ - F_{my1}R_{b1} - m_{A1}gR_{b1} + F_1R_{b1} \end{cases} \tag{22}$$

$$\begin{cases} m_3\ddot{x}_3 + c_{x3}(\dot{x}_3 - \dot{x}_{A2}) + c_{x13}(\dot{x}_3 - \dot{x}_1) + k_{x3}(x_3 - x_{A2}) + k_{x13}(x_3 - x_{A2}) \\ = -F_{mx2} \\ m_3\ddot{y}_3 + c_{y3}(\dot{y}_3 - \dot{y}_{A2}) + c_{y13}(\dot{y}_3 - \dot{y}_1) + k_{y3}(y_3 - x_{A2}) + k_{y13}(y_3 - y_{A2}) \\ = -F_{my2} - m_{A2}g + F_3 \\ m_3\ddot{z}_3 + c_{z3}(\dot{z}_3 - \dot{z}_{A2}) + c_{z13}(\dot{z}_3 - \dot{z}_1) + k_{z3}(z_3 - z_{A2}) + k_{z13}(z_3 - z_{A2}) \\ = -F_{mz2} \\ I_3\ddot{\theta}_3 + c_{t13}(\dot{\theta}_3 - \dot{\theta}_1) + c_{t3}\dot{\theta}_3 + k_{t13}(\theta_3 - \theta_1) + k_{t3}\theta_3 = T_3 - F_{my2}R_{b3} \\ - m_{A2}gR_{b3} + F_3R_{b3} \end{cases} \tag{23}$$

$$\begin{cases} m_2\ddot{x}_2 + c_{x2}(\dot{x}_2 - \dot{x}_{B1}) + c_{x24}(\dot{x}_2 - \dot{x}_4) + k_{x2}(x_2 - x_{B1}) + k_{x24}(x_2 - x_{B1}) \\ = F_{mx1} \\ m_2\ddot{y}_2 + c_{y2}(\dot{y}_2 - \dot{y}_{B1}) + c_{y24}(\dot{y}_2 - \dot{y}_4) + k_{y2}(y_2 - x_{B1}) + k_{y24}(y_2 - y_{B1}) \\ = F_{my1} - m_{B1}g - F_2 \\ m_2\ddot{z}_2 + c_{z2}(\dot{z}_2 - \dot{z}_{B1}) + c_{z24}(\dot{z}_2 - \dot{z}_4) + k_{z2}(z_2 - z_{B1}) + k_{z24}(z_2 - z_{B1}) \\ = F_{mz1} \\ I_2\ddot{\theta}_2 + c_{t24}(\dot{\theta}_2 - \dot{\theta}_4) + c_{t2}\dot{\theta}_2 + k_{t24}(\theta_2 - \theta_4) + k_{t2}\theta_2 = -T_2 - F_{my1}R_{b2} \\ - m_{B1}gR_{b2} + F_2R_{b2} \end{cases} \tag{24}$$

$$\begin{cases} m_4\ddot{x}_4 + c_{x4}(\dot{x}_4 - \dot{x}_{B2}) + c_{x24}(\dot{x}_4 - \dot{x}_2) + k_{x4}(x_4 - x_{B2}) + k_{x24}(x_4 - x_{B2}) \\ = F_{mx2} \\ m_4\ddot{y}_4 + c_{y4}(\dot{y}_4 - \dot{y}_{B2}) + c_{y24}(\dot{y}_4 - \dot{y}_2) + k_{y4}(y_4 - x_{B2}) + k_{y24}(y_4 - y_{B2}) \\ = F_{my2} - m_{B2}g - F_4 \\ m_4\ddot{z}_4 + c_{z4}(\dot{z}_4 - \dot{z}_{B2}) + c_{z24}(\dot{z}_4 - \dot{z}_2) + k_{z4}(z_4 - z_{B2}) + k_{z24}(z_4 - z_{B2}) \\ = F_{mz2} \\ I_4\ddot{\theta}_4 + c_{t24}(\dot{\theta}_4 - \dot{\theta}_2) + c_{t4}\dot{\theta}_4 + k_{t24}(\theta_4 - \theta_2) + k_{t4}\theta_4 = -T_4 - F_{my2}R_{b4} \\ - m_{B2}gR_{b4} + F_4R_{b4} \end{cases} \tag{25}$$

$$\begin{cases} m_{A1}\ddot{x}_{A1} + c_{x1}(\dot{x}_{A1} - \dot{x}_1) + c_{xA1}\dot{x}_{A1} + k_{x1}(x_{A1} - x_1) = -F_{bxA1} \\ m_{A1}\ddot{y}_{A1} + c_{y1}(\dot{y}_{A1} - \dot{y}_1) + c_{yA1}\dot{y}_{A1} + k_{y1}(y_{A1} - y_1) = -F_{byA1} - m_Ag \end{cases} \tag{26}$$

$$\begin{cases} m_{A2}\ddot{x}_{A2} + c_{x3}(\dot{x}_{A2} - \dot{x}_3) + c_{xA2}\dot{x}_{A2} + k_{x3}(x_{A2} - x_3) = -F_{bxA2} \\ m_{A2}\ddot{y}_{A2} + c_{y3}(\dot{y}_{A2} - \dot{y}_3) + c_{yA2}\dot{y}_{A2} + k_{y3}(y_{A2} - y_3) = -F_{byA2} - m_{A2}g \end{cases} \tag{27}$$

$$\begin{cases} m_{B1}\ddot{x}_{B1} + c_{x2}(\dot{x}_{A1} - \dot{x}_2) + c_{xB1}\dot{x}_{B1} + k_{x2}(x_{B1} - x_2) = -F_{bxB1} \\ m_{B1}\ddot{y}_{B1} + c_{y2}(\dot{y}_{B1} - \dot{y}_2) + c_{yB1}\dot{y}_{B1} + k_{y2}(y_{B1} - y_2) = -F_{byB1} - m_{B1}g \end{cases} \tag{28}$$

$$\begin{cases} m_{B2}\ddot{x}_{B2} + c_{x4}(\dot{x}_{B2} - \dot{x}_4) + c_{xB2}\dot{x}_{B2} + k_{x4}(x_{B2} - x_4) = -F_{bxB2} \\ m_{B2}\ddot{y}_{B2} + c_{y4}(\dot{y}_{B2} - \dot{y}_4) + c_{yB2}\dot{y}_{B2} + k_{y4}(y_{B2} - y_4) = -F_{byB2} - m_{B2}g \end{cases}, \tag{29}$$

where g is the acceleration of gravity, F_{mij} ($i=x, y, z; j=1, 2, 3, 4$) is the meshing force of helical gear pair; F_{bij} ($i=x, y; j=A_1, A_2, B_1, B_2$) is the bearing force of each bearing.

To improve the calculation speed and accuracy, it is necessary to conduct dimensionless treatment to the system vibration differential equation. Replace the torsional displacement of (22), (23), (24) and (25) with the meshing line displacement:

$$\begin{cases} m_{e1}\ddot{x}_{n1} = m_{e1}(\ddot{x}_1 - \ddot{x}_2)\sin\alpha_n + m_{e1}(\ddot{y}_1 - \ddot{y}_2)\cos\alpha_n\cos\beta \\ +m_{e1}(\ddot{z}_1 - \ddot{z}_2)\cos\alpha_n\sin\beta - k_{m1}f(x_{n1}) - c_{m1}\dot{x}_{n1} + F_1 + e_1\omega_{m1}^2\sin\omega_{m1}^2 t \\ m_{e2}\ddot{x}_{n2} = m_{e2}(\ddot{x}_3 - \ddot{x}_4)\sin\alpha_n + m_{e2}(\ddot{y}_3 - \ddot{y}_4)\cos\alpha_n\cos\beta \\ +m_{e2}(\ddot{z}_3 - \ddot{z}_4)\cos\alpha_n\sin\beta - k_{m2}f(x_{n2}) - c_{m2}\dot{x}_{n2} + F_2 + e_2\omega_{m2}^2\sin\omega_{m2}^2 t \end{cases}. \tag{30}$$

Among them, meshing line 1 is the meshing line of the right helical gear pair, and meshing line 2 is the meshing line of the left helical gear pair. m_{ei} ($i=1, 2$) is the equivalent mass, F_i ($i=1, 2$) is the external load, and the calculation method is shown by the following equation:

$$\begin{cases} m_{e1} = \dfrac{J_1 J_2}{J_1 r_2^2 + J_2 r_1^2} \\ m_{e2} = \dfrac{J_3 J_4}{J_3 r_4^2 + J_4 r_3^2} \\ F_i = \dfrac{T_j(t)}{r_j}(i = 1, 2; j = 1, 3) \end{cases}. \tag{31}$$

Among them, J_i ($i=1, 2, 3, 4$) is the rotational inertia of each gear, and r_i ($i=1, 2, 3, 4$) is the radius of each gear dividing circle. The tooth side clearance b_m is taken for dimensionless processing of the dynamic differential equation. The results are as follows:

$$\begin{cases} \ddot{\bar{x}}_{n1} = (\ddot{\bar{x}}_1 - \ddot{\bar{x}}_2)\sin\alpha_n + (\ddot{\bar{y}}_1 - \ddot{\bar{y}}_2)\cos\alpha_n\cos\beta + (\ddot{\bar{z}}_1 - \ddot{\bar{z}}_2)\cos\alpha_n\sin\beta \\ - \kappa_{m1}f(\bar{x}_{n1}) - \xi_{m1}\dot{\bar{x}}_{n1} + f_1 + f_{e1} \\ \ddot{\bar{x}}_{n2} = (\ddot{\bar{x}}_3 - \ddot{\bar{x}}_4)\sin\alpha_n + (\ddot{\bar{y}}_3 - \ddot{\bar{y}}_4)\cos\alpha_n\cos\beta + (\ddot{\bar{z}}_3 - \ddot{\bar{z}}_4)\cos\alpha_n\sin\beta \\ - \kappa_{m2}f(\bar{x}_{n2}) - \xi_{m2}\dot{\bar{x}}_{n2} + f_1 + f_{e2} \end{cases} \tag{32}$$

$$\begin{cases} \ddot{\bar{x}}_1 + \xi_{x1}(\dot{\bar{x}}_1 - \dot{\bar{x}}_{A1}) + \xi_{x13}(\dot{\bar{x}}_1 - \dot{\bar{x}}_3) + \xi_{x1}(\bar{x}_1 - \bar{x}_{A1}) + \xi_{x13}(\bar{x}_1 - \bar{x}_{A1}) \\ = (-\kappa_{m1}f(\bar{x}_{n1}) - \xi_{m1}\dot{\bar{x}}_{n1})\sin\alpha_n\ddot{\bar{y}}_1 + \xi_{y1}(\dot{\bar{y}}_1 - \dot{\bar{y}}_{A1}) \\ + \xi_{y13}(\dot{\bar{y}}_1 - \dot{\bar{y}}_3) + \kappa_{y1}(\bar{y}_1 - \bar{x}_{A1}) + \kappa_{y13}(\bar{y}_1 - \bar{y}_{A1}) \\ = (-\kappa_{m1}f(\bar{x}_{n1}) - \xi_{m1}\dot{\bar{x}}_{n1})\cos\alpha_n\cos\beta - f_g \\ \ddot{\bar{z}}_1 + \xi_{z1}(\dot{\bar{z}}_1 - \dot{\bar{z}}_{A1}) + \xi_{z13}(\dot{\bar{z}}_1 - \dot{\bar{z}}_3) + \kappa_{z1}(\bar{z}_1 - \bar{z}_{A1}) + \kappa_{z13}(\bar{z}_1 - \bar{z}_{A1}) \\ = (-\kappa_{m1}f(\bar{x}_{n1}) - \xi_{m1}\dot{\bar{x}}_{n1})\cos\alpha_n\sin\beta \end{cases} \tag{33}$$

$$\begin{cases} \ddot{\bar{x}}_2 + \xi_{x2}(\dot{\bar{x}}_2 - \dot{\bar{x}}_{B1}) + \xi_{x24}(\dot{\bar{x}}_2 - \dot{\bar{x}}_4) + \kappa_{x2}(\bar{x}_2 - \bar{x}_{B1}) + \kappa_{x24}(\bar{x}_2 - \bar{x}_{B1}) \\ = (-\kappa_{m1}f(\bar{x}_{n1}) - \xi_{m1}\dot{\bar{x}}_{n1})\sin\alpha_n\ddot{\bar{y}}_2 + \xi_{y2}(\dot{\bar{y}}_2 - \dot{\bar{y}}_{B1}) \\ + \xi_{y24}(\dot{\bar{y}}_2 - \dot{\bar{y}}_4) + \kappa_{y2}(\bar{y}_2 - \bar{x}_{B1}) + \kappa_{y24}(\bar{y}_2 - \bar{y}_{B1}) \\ = (-\kappa_{m1}f(\bar{x}_{n1}) - \xi_{m1}\dot{\bar{x}}_{n1})\cos\alpha_n\cos\beta - f_g \\ \ddot{\bar{z}}_2 + \xi_{z2}(\dot{\bar{z}}_2 - \dot{\bar{z}}_{B1}) + \xi_{z24}(\dot{\bar{z}}_2 - \dot{\bar{z}}_4) + \kappa_{z2}(\bar{z}_2 - \bar{z}_{B1}) + \kappa_{z24}(\bar{z}_2 - \bar{z}_{B1}) \\ = (-\kappa_{m1}f(\bar{x}_{n1}) - \xi_{m1}\dot{\bar{x}}_{n1})\cos\alpha_n\sin\beta \end{cases} \tag{34}$$

$$\begin{cases} \ddot{\bar{x}}_3 + \xi_{x3}(\dot{\bar{x}}_3 - \dot{\bar{x}}_{A2}) + \xi_{x13}(\dot{\bar{x}}_3 - \dot{\bar{x}}_1) + \kappa_{x3}(\bar{x}_3 - \bar{x}_{A2}) + \kappa_{x13}(\bar{x}_3 - \bar{x}_{A2}) \\ = (-\kappa_{m2}f(\bar{x}_{n2}) - \xi_{m2}\dot{\bar{x}}_{n2})\sin\alpha_n\ddot{\bar{y}}_3 + \xi_{y3}(\dot{\bar{y}}_3 - \dot{\bar{y}}_{A2}) + \xi_{y13}(\dot{\bar{y}}_3 - \dot{\bar{y}}_1) \\ + \kappa_{y3}(\bar{y}_3 - \bar{x}_{A2}) + \kappa_{y13}(\bar{y}_3 - \bar{y}_{A2}) \\ = (-\kappa_{m2}f(\bar{x}_{n2}) - \xi_{m2}\dot{\bar{x}}_{n2})\cos\alpha_n\cos\beta - f_g \\ \ddot{\bar{z}}_3 + \xi_{z3}(\dot{\bar{z}}_3 - \dot{\bar{z}}_{A2}) + \xi_{z13}(\dot{\bar{z}}_3 - \dot{\bar{z}}_1) + \kappa_{z3}(\bar{z}_3 - \bar{z}_{A2}) + \kappa_{z13}(\bar{z}_3 - \bar{z}_{A2}) \\ = (-\kappa_{m2}f(\bar{x}_{n2}) - \xi_{m2}\dot{\bar{x}}_{n2})\cos\alpha_n\sin\beta \end{cases} \tag{35}$$

$$\begin{cases} \ddot{\bar{x}}_4 + \xi_{x4}(\dot{\bar{x}}_4 - \dot{\bar{x}}_{B2}) + \xi_{x24}(\dot{\bar{x}}_4 - \dot{\bar{x}}_2) + \kappa_{x4}(\bar{x}_4 - \bar{x}_{B2}) + \kappa_{x24}(\bar{x}_4 - \bar{x}_{B2}) \\ = (-\kappa_{m2}f(\bar{x}_{n2}) - \xi_{m2}\dot{\bar{x}}_{n2})\sin\alpha_n\ddot{\bar{y}}_4 + \xi_{y4}(\dot{\bar{y}}_4 - \dot{\bar{y}}_{B2}) + \xi_{y24}(\dot{\bar{y}}_4 - \dot{\bar{y}}_2) \\ + \kappa_{y4}(\bar{y}_4 - \bar{x}_{B2}) + \kappa_{y24}(\bar{y}_4 - \bar{y}_{B2}) = (-\kappa_{m2}f(\bar{x}_{n2}) - \xi_{m2}\dot{\bar{x}}_{n2})\cos\alpha_n\cos\beta - f_g \\ \ddot{\bar{z}}_4 + \xi_{z4}(\dot{\bar{z}}_4 - \dot{\bar{z}}_{B2}) + \xi_{z24}(\dot{\bar{z}}_4 - \dot{\bar{z}}_2) + \kappa_{z4}(\bar{z}_4 - \bar{z}_{B2}) + \kappa_{z24}(\bar{z}_4 - \bar{z}_{B2}) \\ = (-\kappa_{m2}f(\bar{x}_{n2}) - \xi_{m2}\dot{\bar{x}}_{n2})\cos\alpha_n\sin\beta \end{cases} \tag{36}$$

In the formula

$$\bar{x}_i = x_i/b_m,\ \bar{y}_i = y_i/b_m,\ \bar{z}_i = z_i/b_m,\ f(\bar{x}_{ni}) = f(\bar{x}_{ni})/b_m$$
$$= \begin{cases} \bar{x}_{ni} - 1, \bar{x}_{ni} > 1 \\ 0, |\bar{x}_{ni}| < 1 \\ \bar{x}_{ni} + 1, \bar{x}_{ni} < -1 \end{cases}, \tau = \omega_n t, \omega_n = \sqrt{\frac{K_a}{m_e}},$$
$$\omega_{ji} = \sqrt{\frac{K_{ji}}{m_{ji}}},\ \kappa_{ji} = \frac{\omega_{ij}^2}{\omega_n^2},\ \kappa_{mi} = \frac{\omega_{ji}^2}{\omega_n^2}\kappa(\tau),\ \kappa(\tau) = \frac{K_{mv}(t)}{K_a},$$
$$\xi_{ji} = \frac{C_{ji}}{2m_i\omega_n},\ \xi_{mv} = \frac{C_{mv}}{2m_{ev}\omega_n},\ f = \frac{F\cos\alpha_n}{m_{ev}b_m\omega_n^2},$$
$$f_g = \frac{g}{b_m\omega_n^2}, f_{ev} = \frac{\mathrm{d}^2 e_v(\tau)/\mathrm{d}\tau^2}{b_m}(i = 1, 2, 3, 4; v = 1, 2; j = x, y, z).$$

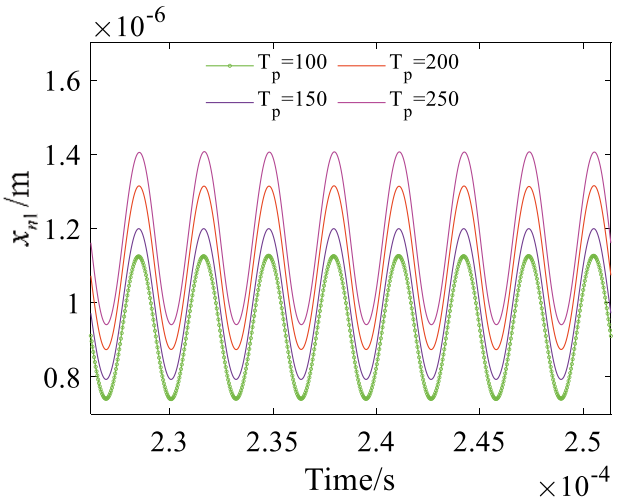

(a) Time-displacement diagram of meshing line 1

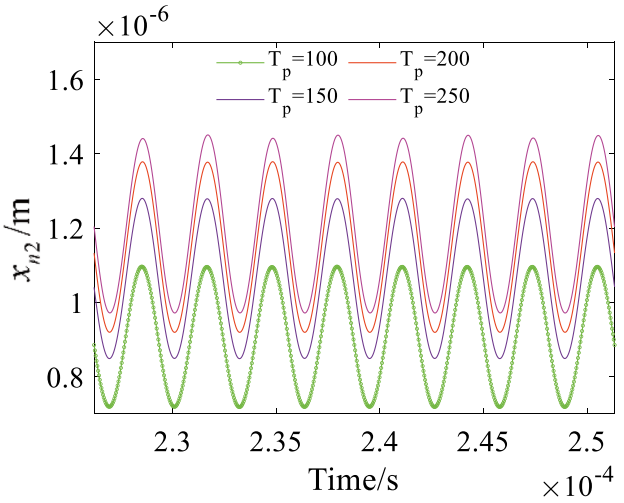

(b) Time-displacement diagram of meshing line 2

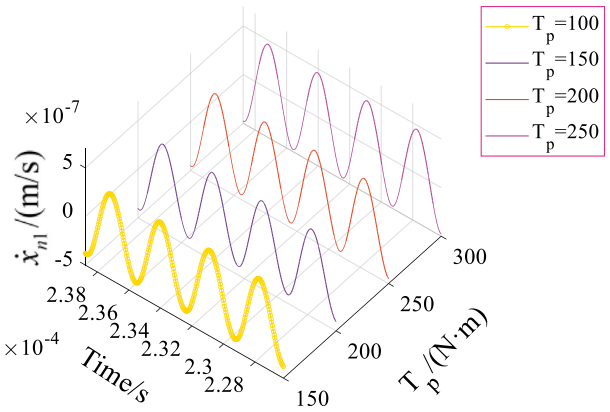

(c) Time-speed diagram of Meshing line 1

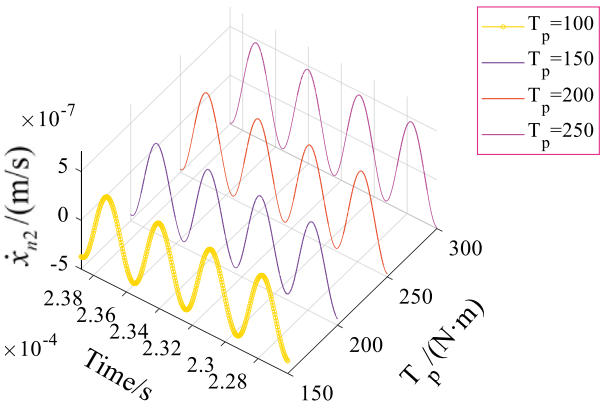

(d) Time-speed diagram of Meshing line 2

Fig. 9 System response under different torques

System Dynamic Response

System Response Under Different Torques

This part explores the nonlinear response of the herringbone gear system under different input torque T_p. The value of T_p is equal to the sum of the value of $T1$ and $T3$. Keep the other system parameters unchanged, change T_p value, and observe the nonlinear response of displacement of meshing line 1 and meshing line 2, respectively. It can be seen from Fig. 9a, b that changing the value of T_p does not change the trajectory trend of the vibration displacement curve, so the changing trend of speed is also unchanged, as shown in Fig. 9c, d. When T_p increases slowly, the average vibration displacement of the meshing line increases, and the amplitude increases slowly. When the input torque changes from 100 to 250 N m, the vibration displacement peaks of meshing line 1 are 1.13 μm, 1.2 μm, 1.3 μm and 1.4 μm, respectively, and the vibration displacement peaks of meshing line 2 are 1.1 μm, 1.28 μm, 1.37 μm and 1.44 μm, respectively. From the velocity–displacement image, it can be seen that meshing line 1 and meshing line 2 have almost the same movement trend under different torques, so the peak of acceleration is almost the same, about 2.5 μm/s.

System Response Under Different Meshing Damping

This part explores the nonlinear response of the herringbone gear system under different meshing damping coefficients

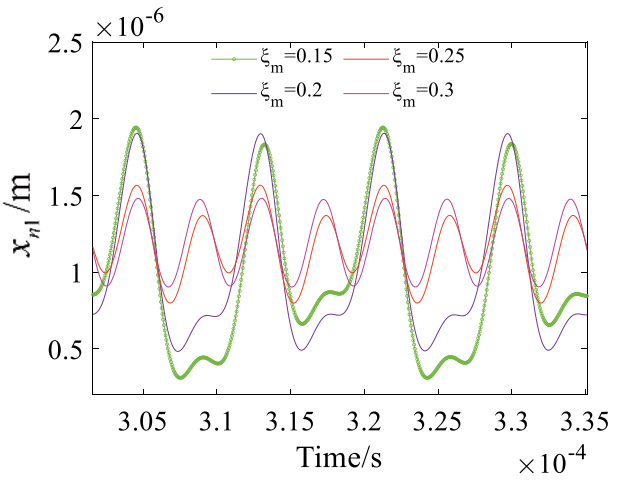

(a) Time-displacement diagram of meshing line 1

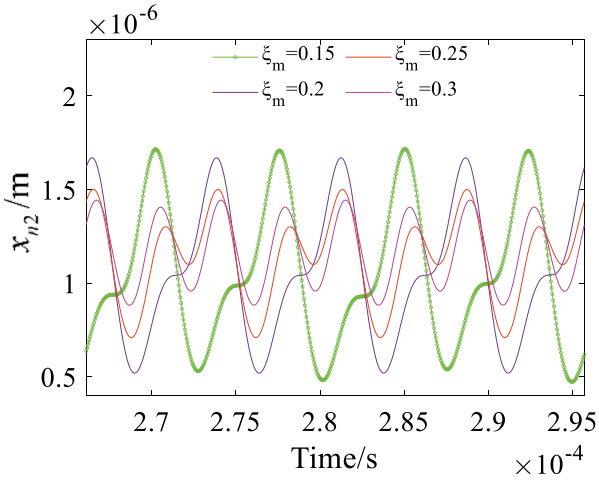

(b) Time-displacement diagram of meshing line 2

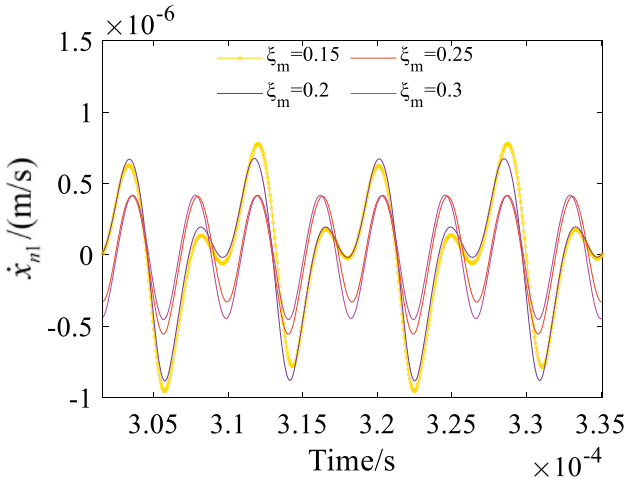

(c) Time-speed diagram of Meshing line 1

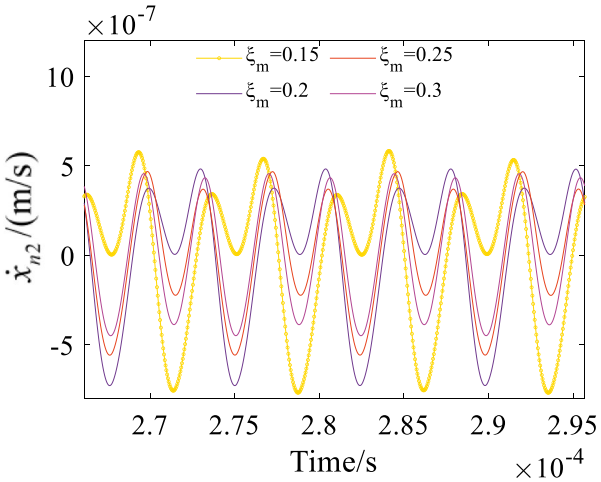

(d) Time-speed diagram of Meshing line 2

Fig. 10 System response under different meshing damping

ξ_m. Keep other system parameters unchanged, change ξ_m value, and observe the meshing line 1 nonlinear displacement and meshing line 2 nonlinear displacement, respectively. By analyzing Fig. 10a, b, it can be seen that changing the value of ξ_m will change the trajectory trend of the vibration displacement curve. As shown in Fig. 10a, b, slowly increasing ξ_m, the vibration displacement of the meshing line gradually changes from stable single-period motion to double-period motion and multi-period motion, and the vibration amplitude gradually increases. When the meshing damping ratio changes from 0.15 to 0.3, the peak of vibration velocity of meshing line 1 is 8 μm/s, 6 μm/s, 4.4 μm/s and 4.3 μm/s, respectively, and the peak of vibration velocity of meshing line 2 is 7 μm/s, 4.7 μm/s, 4.5 μm/s and 3.8 μm/s, respectively.

System Response Under Different Backlashes

This part explores how will the nonlinear dynamical behavior of the herringbone gear system change while changing tooth side backlash b_m. Keep other system parameters unchanged, change b_m value, and observe the nonlinear response of the displacement of meshing line 1 and meshing line 2, respectively. It can be seen from Fig. 11a, b that changing the value of b_m will change the trajectory trend of the vibration displacement curve. When b_m increases slowly, the meshing line vibration displacement gradually changes from a stable single-period motion to a double-period motion and a multi-period motion, and the fluctuation amplitude gradually increases. As shown in Fig. 11c, d, when the backlash changes from 1 to 4 μm, the peak value of stable single-period vibration velocity of meshing line

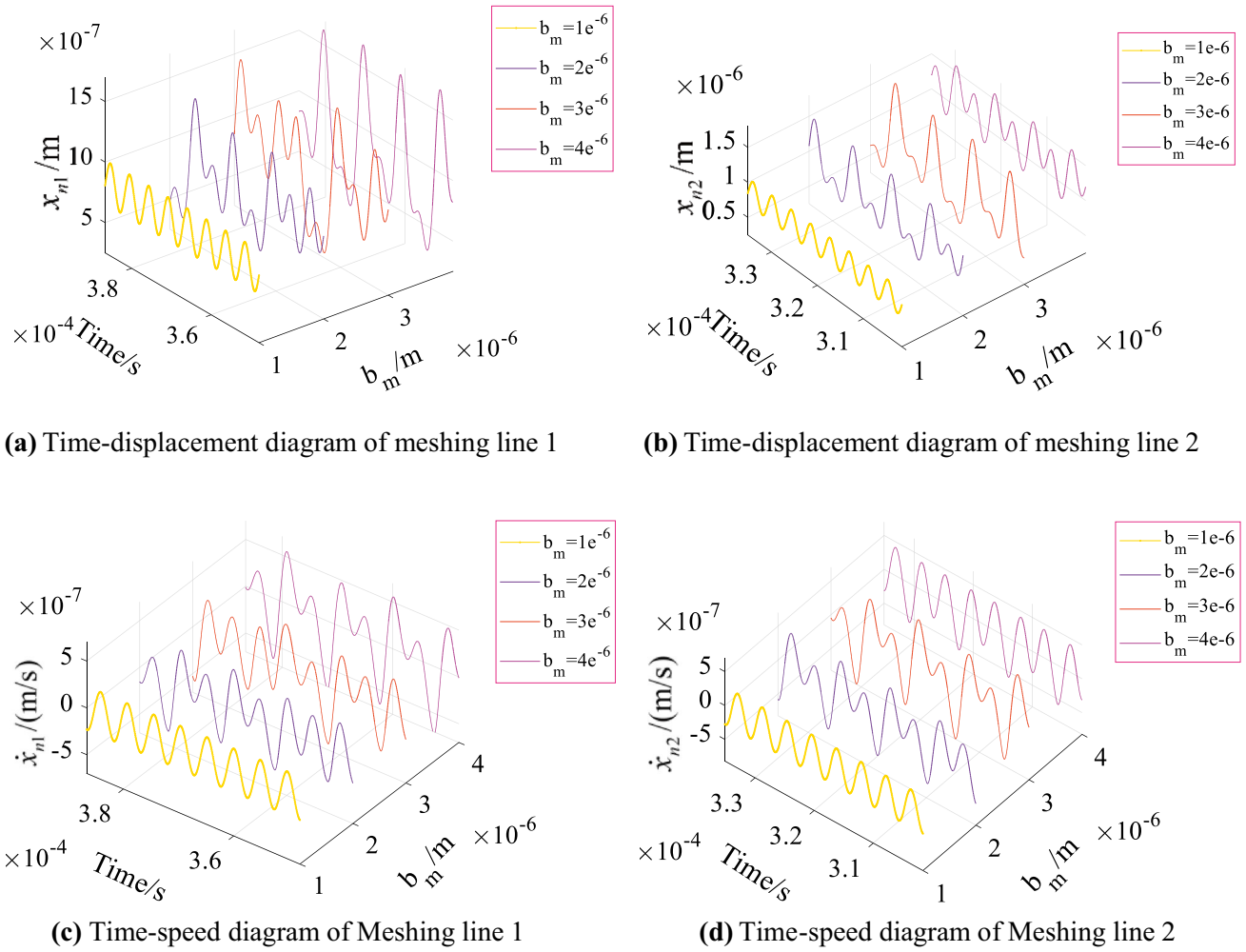

(a) Time-displacement diagram of meshing line 1

(b) Time-displacement diagram of meshing line 2

(c) Time-speed diagram of Meshing line 1

(d) Time-speed diagram of Meshing line 2

Fig. 11 System response under different backlashes

1 is 2.3 μm/s, and the peak value of stable single-period vibration velocity of meshing line 2 is 2.5 μm/s, respectively.

System Response Under Different Meshing Stiffness

This part explores how will the nonlinear dynamical behavior of the herringbone gear system change while changing the mean values of meshing stiffness K_m. Keep the other system parameters unchanged, change the K_m value, and observe the nonlinear response of displacement of meshing line 1 and meshing line 2, respectively. By analyzing Fig. 12a, b, it can be seen that changing the value of K_m will change the trajectory trend of the vibration displacement curve. The vibration displacement of the meshing line is in the chaotic motion state primarily, when K_m increases slowly, it gradually changes to multi-period motion and double-period motion, and finally to stable single-period motion. In this process, the amplitude of velocity fluctuation decreases gradually. As shown in Fig. 12c, d, the peak of vibration velocity of meshing line 1 is 0.43 μm/s and the peak of vibration velocity of meshing line 2 is 0.45 μm/s in the stable motion state.

System Response Under Different Bearing Damping

This part explores how will the nonlinear dynamical behavior of the herringbone gear system change while changing the mean values of bearing damping, The damping of each bearing along the x and y directions is represented by ξ_b. Keep the other system parameters unchanged, change the ξ_b value, and observe the nonlinear response of displacement of meshing line 1 and meshing line 2, respectively. By analyzing Fig. 13a, b, it can be seen that changing the value of ξ_b will change the trajectory trend of the vibration displacement curve. The image is analyzed, and the vibration displacement curve and the vibration velocity curve show that when the bearing damping is low, the system will be in a multi-period motion state and a

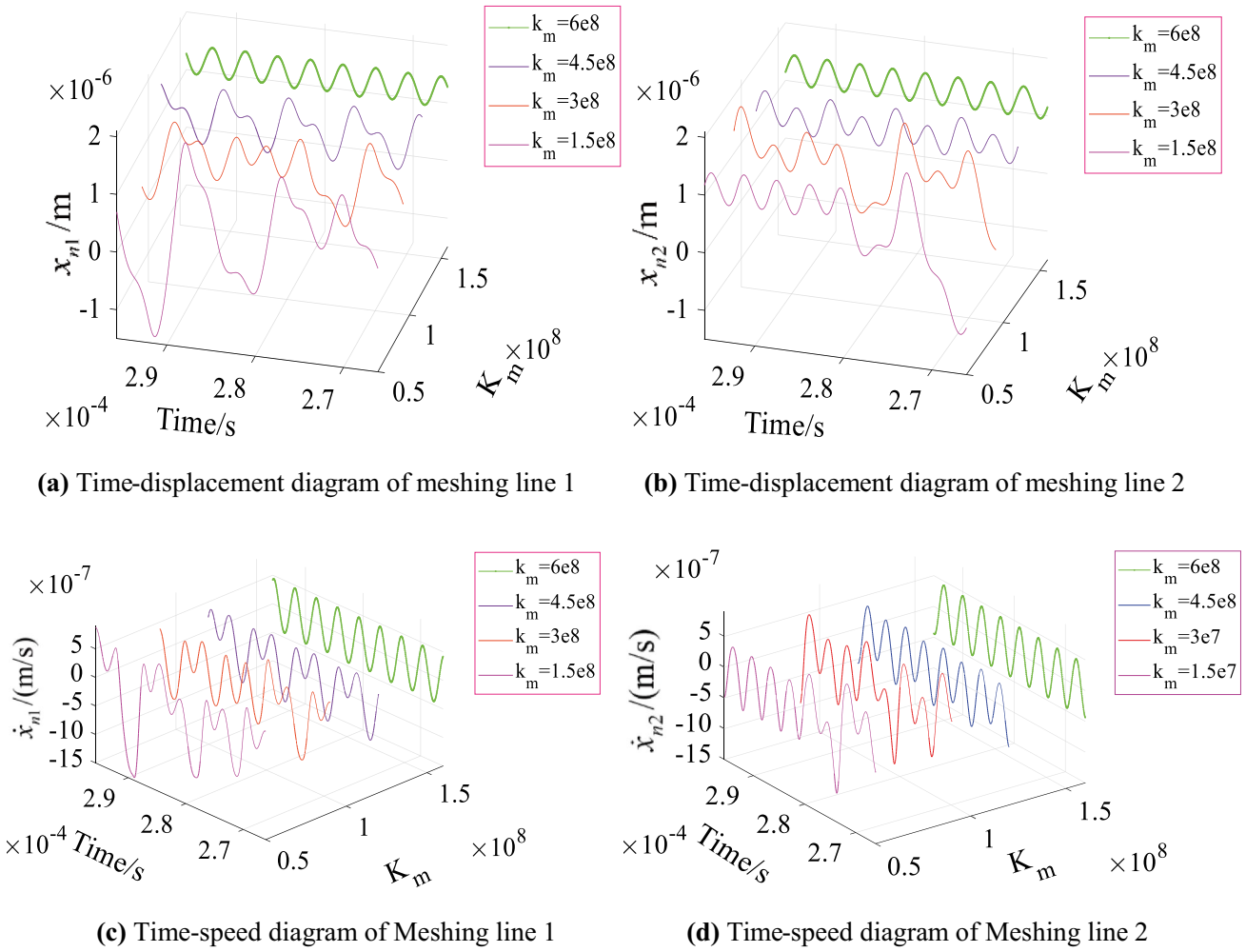

(a) Time-displacement diagram of meshing line 1

(b) Time-displacement diagram of meshing line 2

(c) Time-speed diagram of Meshing line 1

(d) Time-speed diagram of Meshing line 2

Fig. 12 System response under different meshing stiffness

quasi-periodic motion state, and the stability is low. Gradually increasing the bearing damping, the system motion state changes to a stable single-period motion, which indicates that appropriately increasing the bearing damping is beneficial to the system to maintain stability.

System Response Under Different Excitation Frequencies

This part explores how will the nonlinear dynamical behavior of the herringbone gear system change while changing the external load excitation frequency. Taking equivalent displacement as the research object, Fig. 14 shows when the excitation frequency ω_e is 1, 1.55 and 2.2, respectively, What the variation trend of it of meshing line 1 be like. When $\omega_e = 1$, the phase plane is a multi-turn winding trajectory, the points on the Poincaré map are concentrated near two regions, there are two main resonance peaks in the spectrum, and the frequency is between 0.1 and 0.2, it shows that the system is in double periodic motion state. It indicates that the system transits from a stable state to an unstable state. When $\omega_e = 1.55$, the equivalent displacement frequency domain signal on the meshing line has a certain width discrete spectrum, the chaotic frequency is between 0 and 0.4, and its phase plane contains chaotic attractors. The system is doing chaotic motion, which can be shown by the Poincaré map—there are disordered points on the Poincaré map. When $\omega_e = 2.2$, the equivalent displacement phase plane of the meshing line is a orbit, the system is doing Regular periodic motion, which can be shown by the Poincaré map—the Poincaré map only exists one point.

The vibration displacement on the meshing line is analyzed by the wavelet transform method, and the time–frequency diagram at each frequency is shown in Fig. 15. According to the diagram, when $\omega_e = 1$, the main vibration frequency of the meshing displacement is $0.8\omega_e$ and the component is $1.6\omega_e$, and the amplitude is about 0.15 and 0.25, respectively. When $\omega_e = 1.55$, in addition to the

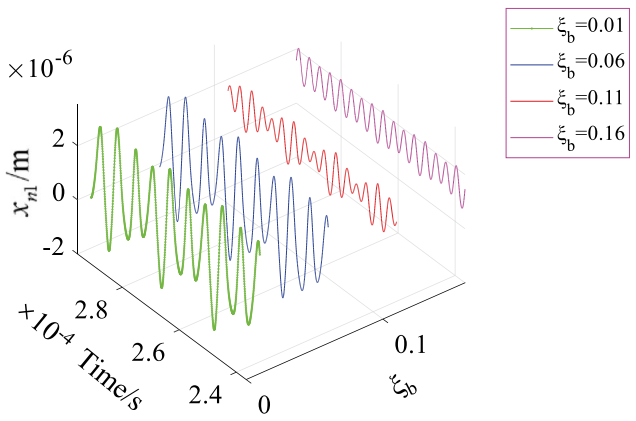

(a) Time-displacement diagram of meshing line 1

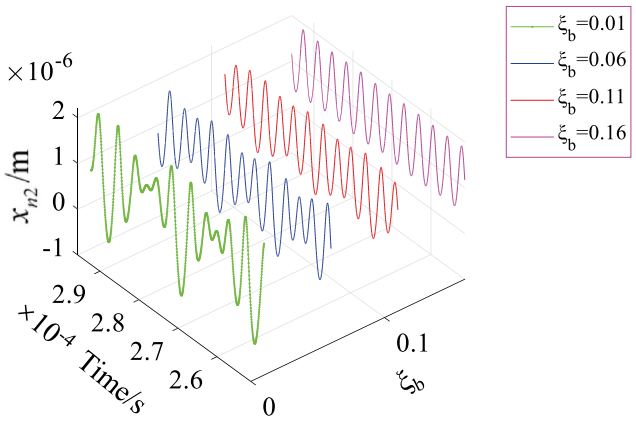

(b) Time-displacement diagram of meshing line 2

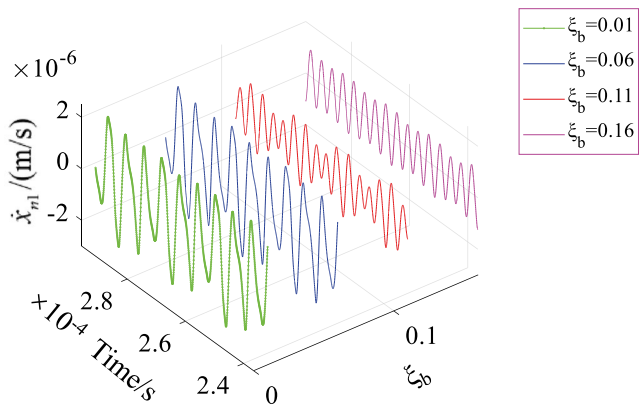

(c) Time-speed diagram of Meshing line 1

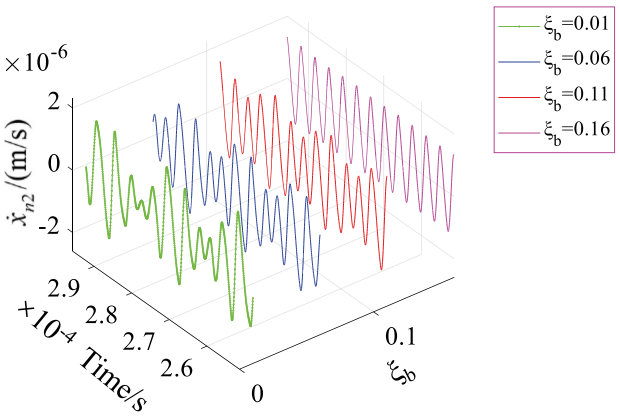

(d) Time-speed diagram of Meshing line 2

Fig. 13 System response under different meshing stiffness

frequency of $0.25\omega_e$, there are more chaotic frequencies, and the amplitude is concentrated at about 0.05, which is consistent with the chaotic motion state of the time history.

The spectrum of the motion space of the system is shown in Fig. 16a. It can be seen that when the excitation frequency is about 1.25 and 1.68, Chaotic motion is what the system is doing. That moment, when system excitation frequency is about 1, the vibration frequency shows a double peak, showing that multi-period motion is the motion that the system is doing. In that case, the system transits from a stable state to an unstable state. In addition, Fig. 16b draws the phase plane and Poincaré image in the spatial state. It can be seen that the system first undergoes multi-period motion, then gradually transitions to chaotic motion, and finally enters a single-period motion. The motion state changes from intermediate to completely unstable, and finally to stable. In Fig. 16, all coordinate values are dimensionless.

While changing the external load excitation frequency ω_e. The data in the diagram shows that when $\omega_e < 0.7$, the system is in a stable one-cycle motion state; when ω_e is between 0.7 and 1.25, the multi-periodic motion is what the system is doing. When ω_e is between 1.25 and 1.72, the system is in a chaotic state; when ω_e is between 1.72 and 1.88, the system is in double-periodic motion. When ω_e is greater than 1.88, the system enters a stable periodic motion again (Fig. 17).

Similar methods can also be used to study the influence of external load excitation frequency on meshing line 2. Taking equivalent displacement as the research object, Fig. 18 shows when the excitation frequency ω_e is 0.9, 1.45 and 2.1, respectively, what the variation trend of it of meshing line 2 be like. When $\omega_e = 0.9$, the phase diagram is a multi-turn winding closed trajectory, and the points on the Poincaré section are concentrated near two regions, It shows that the system is in double periodic motion state. It indicates that the system transits from a stable state to an unstable state.

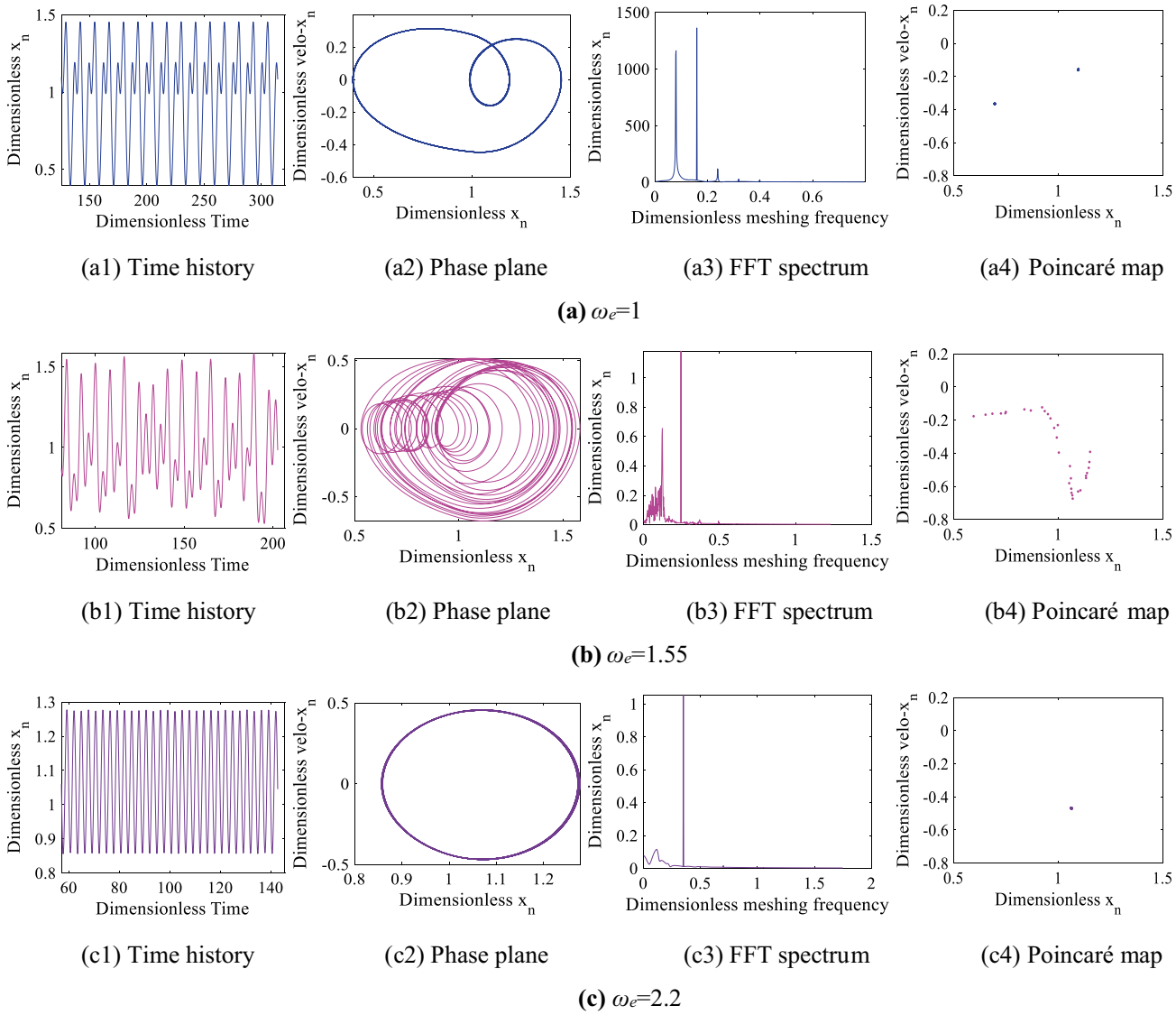

Fig. 14 Changing trend of dynamic response of meshing line 1 under the different excitation frequency

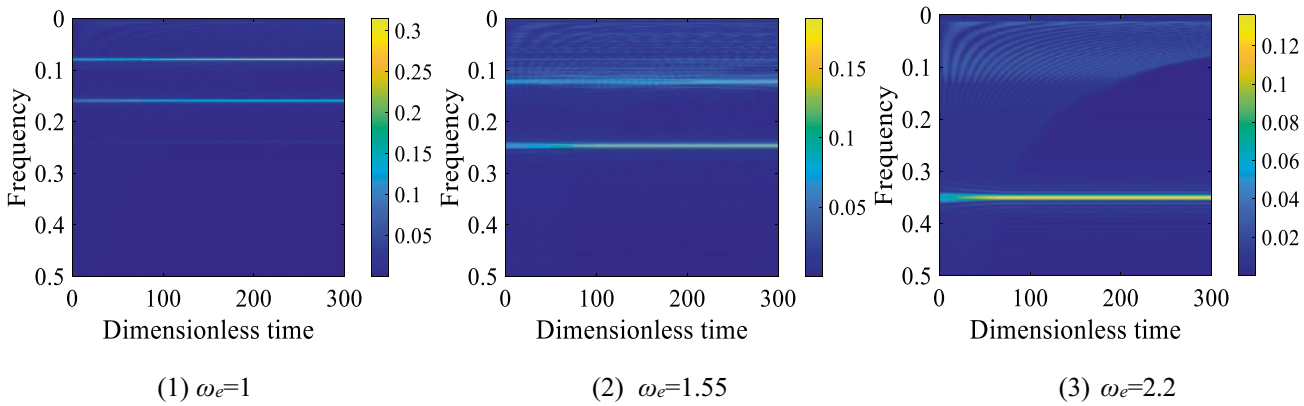

Fig. 15 Meshing line 1 time–frequency diagram of wavelet transform

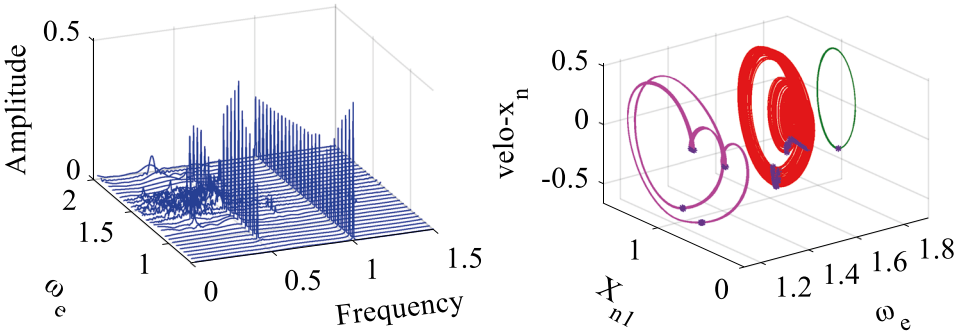

(a) Frequency amplitude of space **(b)** Phase plane and Poincaré of frequency

Fig. 16 Spectrum characteristic of meshing line 1

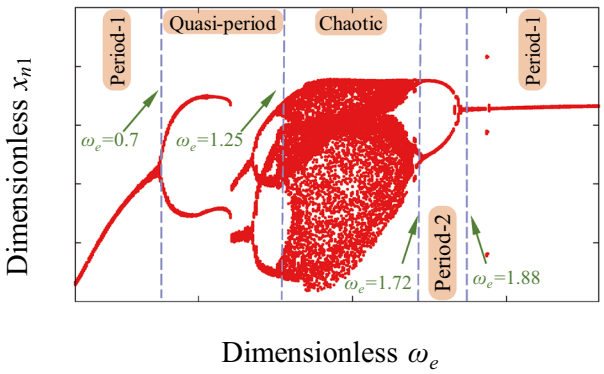

Fig. 17 Bifurcation diagram of meshing line 1

When $\omega_e = 1.45$, the equivalent displacement frequency domain signal on the meshing line has a certain width discrete spectrum, and its phase plane contains chaotic attractors. The system is doing chaotic motion, which can be shown by the Poincaré map—there are disordered points on the Poincaré map.

The vibration displacement on the meshing line is analyzed by the wavelet transform method, and the time–frequency images at each frequency are shown in Fig. 19. According to the FFT image, when $\omega_e = 0.9$, the main vibration frequency of the meshing displacement is $0.7\omega_e$ and the component is $1.5\omega_e$, and the amplitude is about 0.1 and 0.2, respectively. When $\omega_e = 1.45$, in addition to the frequency of $0.23\omega_e$, there are more chaotic frequencies, and the amplitude is concentrated around 0.13, which is consistent with the chaotic motion state of the time history. When $\omega_e = 2.1$, the meshing displacement is mainly composed of $0.35\omega_e$, and the amplitude is about 0.12.

The spectrum of the motion space of the system is shown in Fig. 20a. It can be seen that when the excitation frequency is about 1.25 and 1.68, the vibration frequency of the system appears multi-value phenomenon, showing that chaotic motion is what the system is doing. In that case, when the excitation frequency is about 1, the vibration frequency shows a double peak, showing that multi-period motion is what Herringbone gears system is doing. In addition, from Fig. 20b, it can be seen that the system generally undergoes a state of motion from multi-cycle to chaos to single cycle. In Fig. 20, all coordinate values are dimensionless, the specific dimensionless way is given in the second chapter.

To further study how will the nonlinear dynamical behavior of the herringbone gear system change while changing the external load excitation frequency ω_e, the bifurcation diagram drawing has been drawn, as shown in Fig. 21. The data in the diagram shows that when $\omega_e < 0.63$, the system is in a stable one-cycle motion state; when ω_e is between 0.63 and 1.21, the multi-periodic motion is what the system is doing. When ω_e is between 1.21 and 1.75, the system is in a chaotic state; when ω_e is between 1.75 and 1.9, the system is in double-periodic motion. When ω_e is greater than 1.9, the system enters a stable periodic motion again.

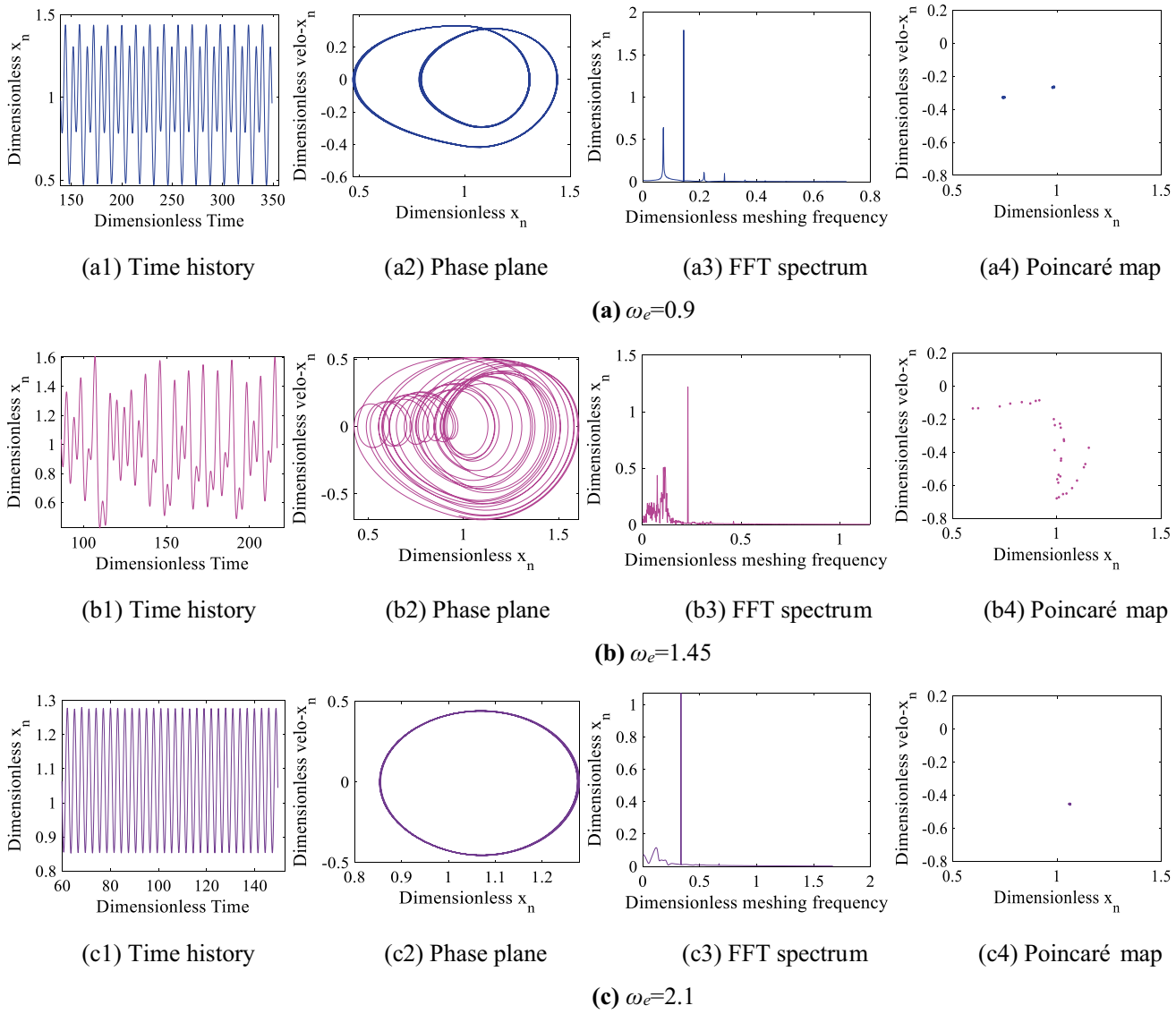

Fig. 18 Changing trend of dynamic response of meshing line 2 under the different excitation frequency

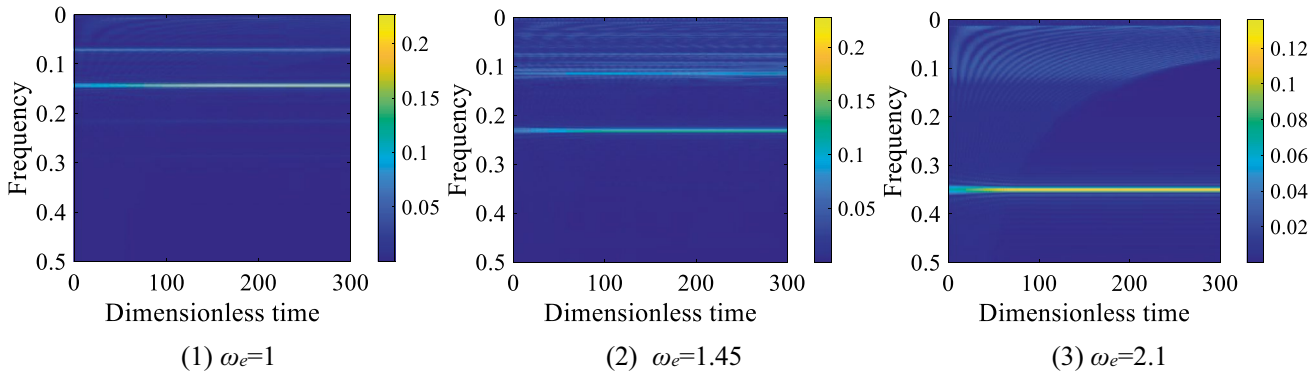

Fig. 19 Meshing line 2 time–frequency diagram of wavelet transform

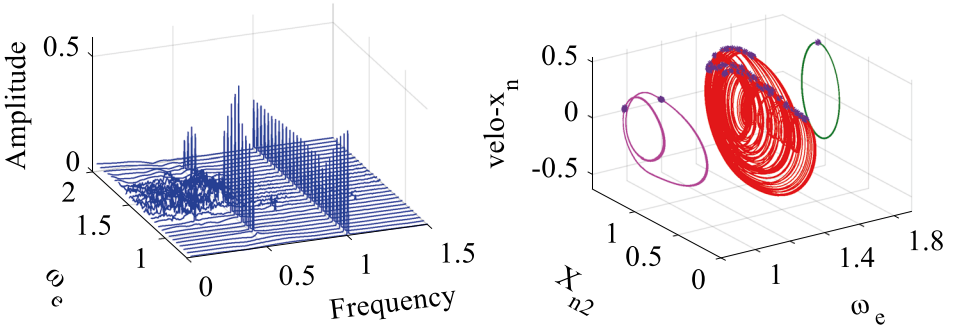

Fig. 20 Spatial spectrum and spatial phase diagram

(a) Frequency amplitude of space **(b)** Phase plane and Poincaré of frequency

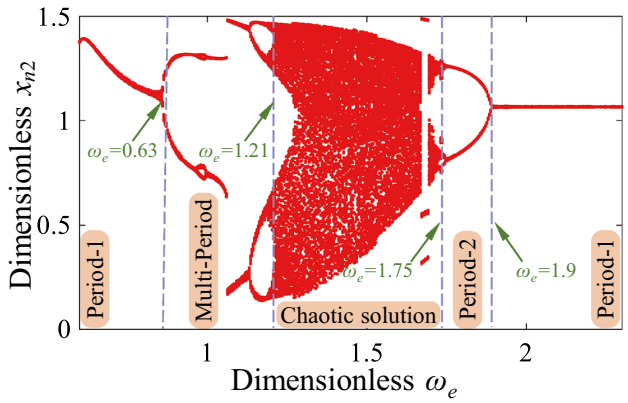

Fig. 21 Bifurcation diagram of meshing line 2

System Main Resonance Analysis

Primary Resonance Used in Analysis of Stability

The characteristics of primary resonance of helical gear pair torsional vibration split by herringbone gear pair are analyzed by multi-scale method. How can excitation load, time-varying meshing stiffness and meshing damping influence the dynamic behavior of herringbone gear system have been studied.

Simplifying Eq. (31), in this case, only taking torsional vibration into account:

$$\ddot{\bar{x}}_n + 2\xi_m \dot{\bar{x}}_n \cos\alpha_t + \kappa(\tau) f(\bar{x}_n)\cos\alpha_t = f_0 - f\cos\omega\tau. \tag{37}$$

In the formula, f_0 represents the dimensionless equivalent static load, and f represents the dimensionless load fluctuation range.

The high-order polynomial fitting of the backlash function, the third-order polynomial accuracy is sufficient:

$$f(\bar{x}_n) = \delta_1 \bar{x}_n + \delta_2 \bar{x}_n^3 = \delta_1(\bar{x}_n + \delta_0 \bar{x}_n^3). \tag{38}$$

The high-order small quantity ε is introduced to represent the variables of time in various scales, as shown in formula (39):

$$T_i = \varepsilon_i \tau \ (i = 0, 1, ...). \tag{39}$$

In different scales, expressing the nonlinear vibration as a time variable function:

$$\bar{x}_n(\tau, \varepsilon) = \sum_{i=1}^{m} \varepsilon^i x_n(T_0, T_1, ..., T_m). \tag{40}$$

In the formula, the highest rank of small parameters has been represented by m, the higher the calculation accuracy, the greater the m value.

Define the partial derivative operator:

$$\frac{\mathrm{d}}{\mathrm{d}\tau} = \sum_{n=1}^{m} \varepsilon^n \frac{\partial}{\partial T_n} = D_0 + \varepsilon D_1 + \cdots + \varepsilon^m D_m \tag{41}$$

$$\frac{\mathrm{d}^2}{\mathrm{d}\tau^2} = \frac{\mathrm{d}}{\mathrm{d}\tau}\left(\sum_{n=1}^{m} \varepsilon^n \frac{\partial}{\partial T_n}\right) = D_0^2 + 2\varepsilon D_0 D_1 + \varepsilon^2(D_1^2 + 2D_0 D_1) + \cdots \tag{42}$$

The gear meshing frequency $\omega = \omega_0 + \omega_1\varepsilon + \omega_2\varepsilon^2 + \ldots$ is defined, system natural frequency has been represented by ω_0. Other parameters of the system can take effective approximate solutions according to the same method. The system parameters $2\xi_m = 2\varepsilon\xi_m$, $\kappa = \varepsilon\kappa$, $\delta_0 = \varepsilon\delta_0$, $f = \varepsilon f$ are redefined.

The mathematical model (43) is re-expressed as

$$\begin{aligned} &\ddot{\bar{x}}_n + 2\varepsilon\xi_m \dot{\bar{x}}_n \cos\alpha_t + (1 + \varepsilon\kappa\cos\omega\tau) \\ &\delta_1(\bar{x}_n + \varepsilon\delta_0 \bar{x}_n^3)\cos\alpha_t = f_0 - \varepsilon f\cos\omega\tau. \end{aligned} \tag{43}$$

The partial derivative operator and the approximate solution are brought into Eq. (44). After the expansion, ε is taken

to the quadratic term. List the differential equations shown in Eqs. (43) and (44):

$$\varepsilon^0 : D_0^2 x_0 + \omega_0^2 x_0 = f_0 \tag{44}$$

$$\varepsilon^1 : D_0^2 x_1 + \omega_0^2 x_1 = f\cos\omega\tau - 2D_0 D_1 x_0 - 2\xi_m D_0 x_0 \cos\alpha_t - \delta_2 x_0^3 \cos\alpha_t - \omega_0^2 \kappa x_0 \cos\alpha_n \cos\omega\tau. \tag{45}$$

Assume that the solution of the 0-order coefficient Eq. (46) is

$$x_0 = A(T_1)e^{i\omega_0 T_0} + f + \overline{A}(T_1)e^{-i\omega_0 T_0}. \tag{46}$$

The excitation frequency offset parameter σ is introduced. Let $\omega = \omega_0 + \varepsilon\sigma$, and rewrite the cosine function with excitation frequency:

$$\cos\omega\tau = \cos(\omega_0\tau + \varepsilon\sigma\tau) = \cos(\omega_0 T_0 + \sigma T_1) = \frac{1}{2}e^{i\sigma T_1}e^{i\omega_0 T_0} + cc, \tag{47}$$

where cc denotes the conjugate plural of its preceding term.

Replace expressions (46) and (47) with ε^1:

$$\begin{aligned} D_0^2 x_1 + \omega_0^2 x_1 = {} & \frac{f}{2}e^{i\sigma T_1}e^{i\omega_0 T_0} - 2iD_1 A\omega_0 e^{i\omega_0 T_0} - 2i\xi_m A\omega_0 e^{i\omega_0 T_0}\cos\alpha_t \\ & - \delta_2\left(\frac{6A\overline{A}f_0 + f_0^3}{2} + A^3 e^{3i\omega_0 T_0} + 3A^2 e^{2i\omega_0 T_0} + 3A^2\overline{A}e^{i\omega_0 T_0} + 3Af_0^2 e^{i\omega_0 T_0}\right)\cos\alpha_t \\ & - \frac{1}{2}\kappa\omega_0^2(Ae^{i\sigma T_1}e^{i\omega_0 T_0} + f_0 e^{i\sigma T_1}e^{i\omega_0 T_0} + Ae^{-i\sigma T_1})\cos\alpha_t + cc. \end{aligned} \tag{48}$$

To avoid perpetual projects, should meet

$$\frac{f}{2}e^{i\sigma T_1} - 2iD_1 A\omega_0 - 3\delta_2 A^2\overline{A}\cos\alpha_t - 3\delta_2 A f_0^2\cos\alpha_t - \frac{1}{2}\kappa\omega_0^2 f_0 e^{i\sigma T_1}\cos\alpha_t = 0. \tag{49}$$

Rewrite equation A, as shown in the following equation:

$$A(T_1) = \frac{1}{2}\alpha(T_1)e^{i\beta(T_1)}. \tag{50}$$

$\alpha(T_1)$ denotes the slow change of system amplitude and $\beta(T_1)$ denotes the slow change of system frequency. Eliminating $e^{i\beta(T_1)}$ on both sides simultaneously and separating the real and imaginary parts:

$$D_1\alpha = -\xi_m\alpha\cos\alpha_t + \frac{1}{2\omega_0}(f - \omega_0^2\kappa f_0\cos\alpha_n)\sin\varphi \tag{51}$$

$$\alpha D_1\varphi = \alpha\sigma - \frac{3\delta_2\alpha^3\cos\alpha_t + 12\delta_2\alpha f_0^2\cos\alpha_t}{8\omega_0} + \frac{1}{2\omega_0}(f - \omega_0^2\kappa f_0\cos\alpha_t)\cos\varphi \tag{52}$$

$\varphi = \beta(T_1) - \sigma T_1$ describes the real phase of the system.

Let $\frac{d\alpha}{d\tau} = \alpha\frac{d\varphi}{d\tau} = 0$, the amplitude and phase satisfy the algebraic equation:

$$\begin{cases} \overline{\alpha}\xi_m\cos\alpha_t = \frac{1}{2\omega_0}(f - \omega_0^2\kappa f_0\cos\alpha_t)\sin\overline{\varphi} \\ \overline{\alpha}\sigma - \frac{3\delta_2\overline{\alpha}^3\cos\alpha_t + 12\delta_2\overline{\alpha}f_0^2\cos\alpha_t}{8\omega_0} = -\frac{1}{2\omega_0}(f - \omega_0^2\kappa f_0\cos\alpha_t)\cos\overline{\varphi} \end{cases}. \tag{53}$$

The amplitude–frequency response equation is shown in Eq. (53):

$$(\xi_m\overline{\alpha}\cos\alpha_n)^2 + \left(\overline{\alpha}\sigma - \frac{3\delta_2\overline{\alpha}^3\cos\alpha_n + 12\delta_2\overline{\alpha}f_0^2\cos\alpha_n}{8\omega_0}\right)^2 = \left(\frac{f - \omega_0^2\kappa f_0\cos\alpha_t}{2\omega_0}\right)^2 \tag{54}$$

$$\overline{\varphi} = \arctan\left(\frac{\overline{\alpha}\xi_m\cos\alpha_t}{\frac{3\delta_2\overline{\alpha}^3\cos\alpha_t + 12\delta_2\overline{\alpha}f_0^2\cos\alpha_t}{8\omega_0} - \overline{\alpha}\sigma}\right). \tag{55}$$

Equations (51) and (52) are linearized to form a differential equation related to the amplitude disturbance $\Delta\alpha$ and the phase disturbance $\Delta\varphi$:

$$\begin{cases} D_1\Delta\alpha = -\Delta\alpha\xi_m\cos\alpha_t + \Delta\varphi\frac{1}{2\omega_0}(f - \omega_0^2\kappa f_0\cos\alpha_t)\cos\overline{\varphi} \\ D_1\Delta\varphi = -\Delta\alpha\left(\frac{3\delta_2\overline{\alpha}\cos\alpha_t}{4\omega_0} + \frac{f - \omega_0^2\kappa f_0\cos\alpha_t}{2\omega_0\overline{\alpha}^2}\cos\overline{\varphi}\right) \\ -\Delta\varphi\frac{f - \omega_0^2\kappa f_0\cos\alpha_t}{2\omega_0\overline{\alpha}^2}\sin\overline{\varphi} \end{cases}. \tag{56}$$

Eliminate $\overline{\varphi}$, system equilibrium equation is shown as follows:

$$\det\begin{bmatrix} -\lambda - \xi_m\cos\alpha_t - \overline{\alpha}\left(\frac{3\delta_2\overline{\alpha}^3\cos\alpha_t + 12\delta_2 f_0^2\cos\alpha_t}{8\omega_0}\right) \\ \frac{1}{\overline{\alpha}}\left(\sigma - \frac{3\delta_2\overline{\alpha}^2\cos\alpha_t + 12\delta_2 f_0^2\cos\alpha_t}{8\omega_0}\right) - \lambda - \xi_m\cos\alpha_t \end{bmatrix}. \tag{57}$$

In summary, when $\xi_m > 0$, the system stability condition is

$$(\xi_m \cos\alpha_t)^2 + \left(\sigma - \frac{3\delta_2\overline{\alpha}^2\cos\alpha_t + 12\delta_2 f_0^2\cos\alpha_t}{8\omega_0}\right)\left(\sigma - \frac{9\delta_2\overline{\alpha}^2\cos\alpha_t + 12\delta_2 f_0^2\cos\alpha_t}{8\omega_0}\right) > 0. \tag{58}$$

Numerical Analysis of Primary Resonance

Discuss how will system primary resonance response change while meshing damping is changing. Define the initial parameters in Eq. (53), meshing damping $\xi_m = 0.05$, dimensionless static load $f = 0.3$, dynamic load fluctuation amplitude $f = 0.3$.

Change the parameter ξ_m and draw the amplitude–frequency diagram, as shown in Fig. 22. When ξ_m is 0.05, 0.07 and 0.09, There are unstable fragments in the curve in the diagram. Increase ξ_m, system main resonance amplitude α decreases, and the unstable fragments gradually shrinks. When ξ_m is 0.12, the curve in the figure is a solid line, indicating that the system is stable. This indicates that when the damping increases, it will help the system to maintain stability. When ω takes different values, changing ξ_m, α will also change. In this case, the curve is drawn to show the trend of α, as shown in Fig. 22b. When ω is 0.4 and 0.75, increase ξ_m will lead to the decrease of the system main resonance amplitude. When ω is 1.25, the amplitude of the system is in the transition stage between stable and unstable, and there is a trend of multi-value jump. When ω is 1.55, the main amplitude of the system is in the unstable stage, and there will be a multi-value jump phenomenon in the shadow part of the graph. At this time, increase ξ_m slowly from 0.2, α will first change from single value to multi-value, and then change back from multi-value to single value. A_1, A_2, A_3, A_4 are the critical points of single-value region and multi-value region, respectively.

Discuss how will system primary resonance response change, while external load is changing. Define the initial parameters in Eq. (53), meshing damping $\xi_m = 0.05$, dimensionless static load $f = 0.3$, dynamic load fluctuation amplitude $f = 0.3$.

Change the parameter external load f and draw the amplitude–frequency diagram, as shown in Fig. 23. When f is 0.4 and 0.9, There are unstable fragments in the curve in the diagram, Represented by dotted line. Decrease f, system main resonance amplitude α decreases, and the unstable fragments gradually shrinks. When f is 0.1 and 0, the curve in the figure are solid lines, indicating that the system is stable. When f is 0.4 and 0.9, the curve in the figure are solid lines, indicating that the system is unstable. This indicates that when the external load decreases, it will help the system to maintain stability. When ω takes different values, changing f, α will also change. In this case, the curve is drawn to show the trend of α, as shown in Fig. 23b. When ω is 0.75, decrease f will lead to the decrease of the system main resonance amplitude. When ω is 1.05, the amplitude of the system is in the transition stage between stable and unstable, and there is a trend of multi-value jump. When ω is 1.25, the main amplitude of the system is in the unstable stage, and there will be a multi-value jump phenomenon in the shadow part of the graph. At this time, increase f slowly from 0.08, α will first change from single value to multi-value.

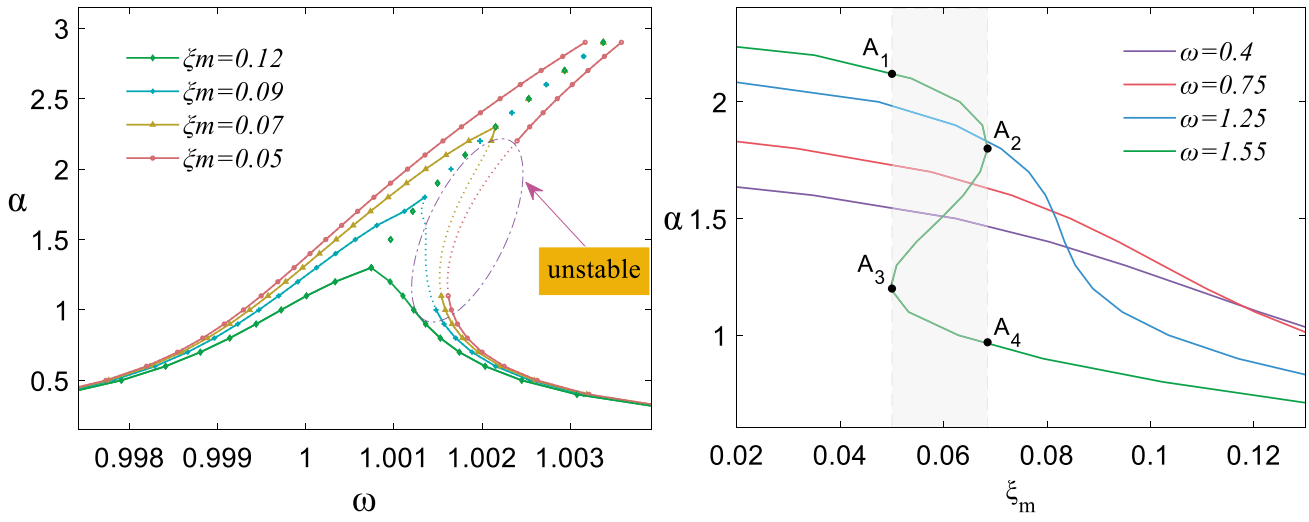

(a) Curves family of ω-α **(b)** Curves family of ξ_m-α

Fig. 22 Main resonance response of meshing damping

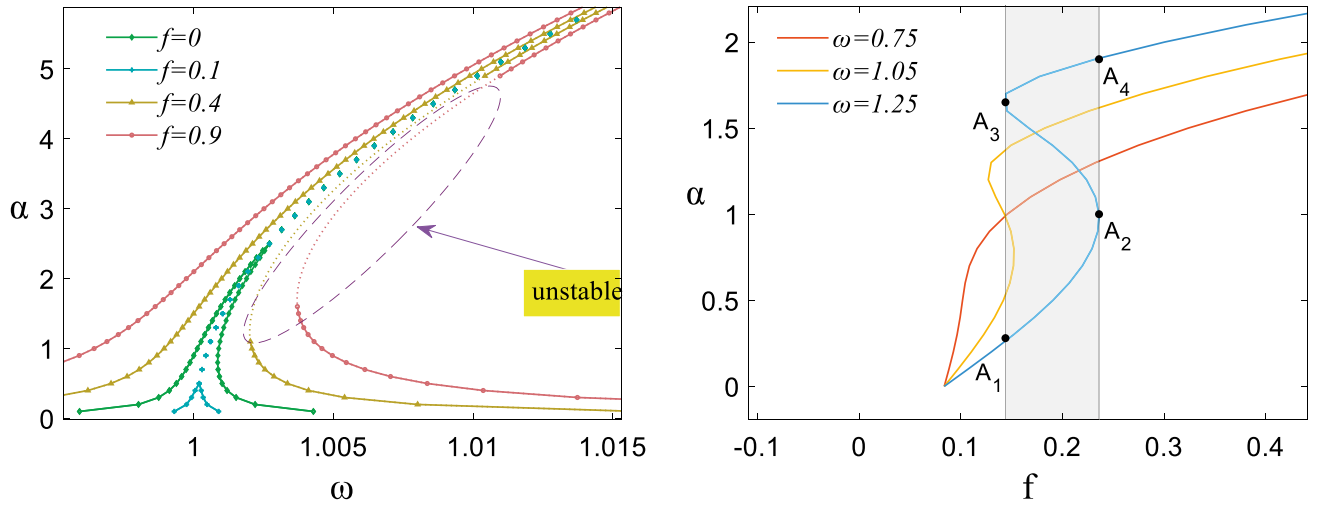

(a) Curves family of ω-α **(b)** Curves family of f-α

Fig. 23 Primary resonance response of load fluctuation

Discuss how will system primary resonance response change, while meshing stiffness is changing. Define the initial parameters in Eq. (53), meshing damping $\xi_m = 0.05$, dimensionless static load $f = 0.3$, dynamic load fluctuation amplitude $f = 0.3$.

Change the parameter meshing stiffness κ and draw the amplitude–frequency diagram, as shown in Fig. 24. When κ is 0.4 and 0.6. There are unstable fragments in the curve in the diagram, the unstable segment is represented by a dotted line in the figure. Increase κ, system main resonance amplitude α decreases, and the unstable fragments gradually shrinks. When κ is 0.8 and 1, the curve in the figure are solid lines, indicating that the system is stable. This indicates that keep other parameters of the system, such as ω unchanged, when the meshing stiffness increases, it will help the system to maintain stability. When ω takes

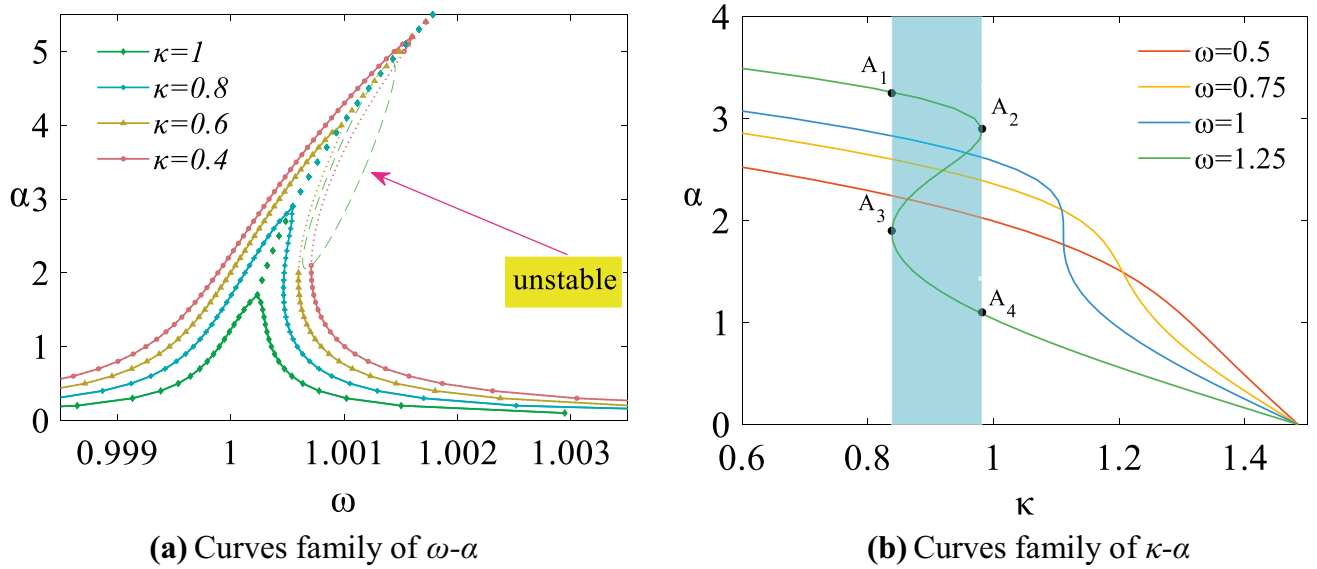

(a) Curves family of ω-α **(b)** Curves family of κ-α

Fig. 24 Primary resonance response of stiffness fluctuation

different values, changing κ, α will also change. In this case, the curve is drawn to show the trend of α, as shown in Fig. 24b. When ω is 0.5, increase κ will lead to the decrease of the system main resonance amplitude, at this time, the stability of nonlinear periodic vibration of the system increases. When ω is 0.75 and 1, the amplitude of the system is in the transition stage between stable and unstable, and there is a trend of multi-value jump. When ω is 1.25, the main amplitude of the system is in the unstable stage, and there will be a multi-value jump phenomenon in the shadow part of the graph. At this time, increase κ slowly from 0.6, α will first change from single value to multi-value, and then change back from multi-value to single value. A_1, A_2, A_3, A_4 are the critical points of single-value region and multi-value region, respectively.

Conclusion

1. The nonlinear dynamic model of herringbone gear is established and its vibration characteristics are analyzed. The results show that the bending-torsion coupled herringbone gear system has rich nonlinear behavior. Keeping other parameters of the system unchanged, changing the excitation frequency, meshing stiffness, backlash, input torque, meshing damping and bearing damping, respectively, the system will experience periodic motion, quasi-periodic motion, multi-periodic motion, chaos and other motion states. When these parameters are not within a reasonable range, the system will fall into chaos and the motion state is unpredictable. This indicates that the system parameters should be reasonably selected, so that it can run stably.
2. The main resonance characteristics of the system are analyzed by the multi-scale method. The results show that increasing the meshing damping ratio is beneficial to suppress the excessive amplitude, which is helpful to reduce the unstable branch and prevent amplitude mutation. One of the factors causing instability of the system is excessive load fluctuation, and the system amplitude is positively correlated with the load amplitude. The system stability is negatively correlated with the external excitation frequency and positively correlated with the meshing stiffness amplitude. Increase the meshing stiffness will reduce the amplitude jump probability and interval of the system and improve its stability.

Acknowledgements This research is financially supported by National Natural Science Foundation of China (No. 52265004), National Key Laboratory of Science and Technology on Helicopter Transmission (No. HTL-0-21G07), Open Fund of State Key Laboratory of Digital Manufacturing Equipment and Technology, Huazhong University of Science and Technology (No. DMETKF2021017), Guangxi Science and Technology Major Program (No. 2023AA19005), and entrepreneurship and Innovation Talent Program of Taizhou City, Jiangsu Province.

Data availability All relevant data are within the paper.

Declarations

Conflict of interest Shuai Mo and Yanjun Zeng contributed equally to this manuscript, and Shuai Mo and Yanjun Zeng are co-first authors of the article. We declare that we have no conflicts with other people or organizations that can inappropriately influence our work.

References

1. Shi J, Gou X, Zhu L (2021) Generation mechanism and evolution of five-state meshing behavior of a spur gear system considering gear-tooth time-varying contact characteristics. Nonlinear Dyn 106(3):2035–2060
2. Cao Z, Chen Z, Jiang H (2020) Nonlinear dynamics of a spur gear pair with force-dependent mesh stiffness. Nonlinear Dyn 99(2):1227–1241
3. Xiang L, Gao N (2017) Coupled torsion–bending dynamic analysis of the gear-rotor-bearing system with eccentricity fluctuation. Appl Math Model 50:569–584
4. Liu P, Zhu L, Gou X et al (2021) Modeling and analyzing of nonlinear dynamics for spur gear pair with pitch deviation under multi-state meshing. Mech Mach Theory 163:104378
5. Chen SY, Tang JY, Luo CW et al (2011) Nonlinear dynamic characteristics of geared rotor bearing systems with dynamic backlash and friction. Mech Mach Theory 46(4):466–478
6. Miroslav B, Vladimír Z (2011) On modeling and vibration of gear drives influenced by nonlinear couplings. Mech Mach Theory 46(3):375–397
7. Mo S, Zhang YX, Song YL et al (2022) Nonlinear vibration and primary resonance analysis of non-orthogonal face gear-rotor-bearing system. Nonlinear Dyn 108:3367–3389
8. Yang J, Zhu R, Yue Y et al (2022) Nonlinear analysis of herringbone gear rotor system based on the surface waviness excitation of journal bearing. J Braz Soc Mech Sci Eng 54:44–52
9. Yi Y, Huang K, Xiong YS, Sang M (2019) Nonlinear dynamic modeling and analysis for a spur gear system with time-varying pressure angle and gear backlash. Mech Syst Signal Process 132:18–34
10. Tatsuhito A, Kensho S (2022) Theoretical analysis of nonlinear vibration characteristics of gear pair with shafts. Theor Appl Mech Lett 12(2):100324
11. Yang Y, Xia WK, Han JM, Song YF, Wang JF, Dai YP (2019) Vibration analysis for tooth crack detection in a spur gear system with clearance nonlinearity. Int J Mech Sci 157:648–661
12. Liu J, Li XB, Pang RK, Xia M (2023) Dynamic modeling and vibration analysis of a flexible gear transmission system. Mech Syst Signal Process 197:110367
13. Liu J, Li XB, Pang RK, Xia M (2023) A dynamic model for the planetary bearings in a double planetary gear set. Mech Syst Signal Process 194:110257
14. Xu X, Jiang G, Wang H et al (2022) Investigation on dynamic characteristics of herringbone planetary gear system considering tooth surface friction. Meccanica 57:1677–1699

15. Mo S, Zhang Y, Luo B et al (2022) The global behavior evolution of non-orthogonal face gear-bearing transmission system. Mech Mach Theory 175:104969
16. Mo S, Zhang T, Jin GG et al (2020) Analytical investigation on load sharing characteristics of herringbone planetary gear train with flexible support and floating sun gear. Mech Mach Theory 144(2):1–27
17. Mo S, Zhang YD, Wu Q (2015) Research on multiple-split load sharing of two-stage star gearing system in consideration of displacement compatibility. Mech Mach Theory 88(1):1–15
18. Mo S, Zhang YD, Wu Q et al (2016) Research on Natural Characteristics of double-helical star gearing system for GTF aeroengine. Mech Mach Theory 106(12):166–189
19. Mo S, Zhou CP, Dang HY (2022) Lubrication effect of the nozzle layout for arc tooth cylindrical gears. J Tribol 144(3):1–25
20. Wang SY, Zhu RP (2022) Modeling and theoretical investigation of nonlinear torsional characteristics for double-helical star gearing system in GTF gearbox. J Vib Eng Technol 10:193–209
21. Wang SY, Zhu RP (2020) Nonlinear torsional dynamics of star gearing transmission system of GTF gearbox. Shock Vib 2020:1–15
22. Tian G, Gao Z, Liu P, Bian Y (2022) Dynamic modeling and stability analysis for a spur gear system considering gear backlash and bearing clearance. Machines 10(6):439
23. Wang W, Cao JY, Dhiman M, Saibal R, Lin J (2018) Comparison of harmonic balance and multi-scale method in characterizing the response of monostable energy harvesters. Mech Syst Signal Process 108:252–261
24. Peng J, Wang L, Zhao Y, Zhao Y (2013) Bifurcation analysis in active control system with time delay feedback. Appl Math Comput 19(219):10073–10081
25. Huang GH, Xu SS, Zhang WH et al (2017) Super-harmonic resonance of gear transmission system under stick-slip vibration in high-speed train. J Cent South Univ 24:726–735
26. Niu J, Shen Y, Yang S, Li S (2018) Higher-order approximate steady-state solutions for strongly nonlinear systems by the improved incremental harmonic balance method. J Vib Control 24(16):3744–3757
27. Shi HR, Zhao DY, Li ZG, Zhang JP (2019) Primary resonance analysis of spur gear with time delay feedback control. Vib Shock 38(21):91–96
28. Wang JG, Bo L, Rui S, Zhao YX (2020) Resonance and stability analysis of a cracked gear system for railway locomotive. Appl Math Model 77(1):253–266
29. Moradi H, Salarieh H (2012) Analysis of nonlinear oscillations in spur gear pairs with approximated modeling of backlash nonlinearity. Mech Mach Theory 51:14–31
30. Celikay A, Donmez A, Kahraman A (2021) An experimental and theoretical study of subharmonic resonances of a spur gear pair. J Sound Vib 515:116421
31. Kandil A, Hamed YS, Mohamed MS, Awrejcewicz J, Bednarek M (2022) Third-order superharmonic resonance analysis and control in a nonlinear dynamical system. Mathematics 10(8):1282
32. Öztürk VY, Cigeroglu E, Özgüven HN (2021) Ideal tooth profile modifications for improving nonlinear dynamic response of planetary gear trains. J Sound Vib 500:116007